Addition of chemotherapy to radiotherapy promotes progenitor-exhausted CD8$^+$ T-cell clonal dominance in head and neck cancer

Charleen Chan Wah Hak[1]*, Anton Patrikeev[1], Antonio Rullan[1,2], Emmanuel C Patin[1], Victoria Roulstone[1], Lisa C Hubbard[1], Matthew Guelbert[3], Elizabeth S Appleton[1], Shane Foo[1], Isaac Dean[1], Amy Burley[1], Joan N Kyula-Currie[1], Holly Baldock[4], Jen Y Lee[1], Pablo Nenclares[1,5], Hannah Nanapragasam[1], Carmen Murano[1], Malin Pedersen[1], Maggie Chon U Cheang[6], Shree Bhide[1,5], Masahiro Ono[7†], Kevin J Harrington[1,5†], Alan A Melcher[1†].

[1]Division of Radiotherapy and Imaging, The Institute of Cancer Research, London SW3 6JB, UK.
[2]Institute of Immunity and Transplantation, University College London.
[3]Flow Cytometry Facility, The Institute of Cancer Research, London SW3 6JB, UK.
[4]Biological Services Unit, The Institute of Cancer Research, London SW3 6JB, UK.
[5]Head and Neck Unit, The Royal Marsden Hospital, London, UK.
[6]Clinical Trials and Statistics Unit at The Institute of Cancer Research (ICR-CTSU)
[7]Faculty of Natural Sciences, Department of Life Sciences, Imperial College London, UK.

*Corresponding author
[†]These authors jointly supervised this work.

Short Title: Chemoradiotherapy promotes progenitor exhausted CD8$^+$ T-cell clonal expansion

Keywords: chemoradiotherapy, head and neck squamous cell carcinoma. CD8$^+$ T-cells. T-cell exhaustion. single-cell transcriptomics.

ABSTRACT

Concomitant chemoradiotherapy (CRT) is a standard-of-care for unresectable locally-advanced head and neck squamous cell carcinoma (LA-SCCHN), but its immune effects, particularly compared to radiotherapy (RT) alone, remain unclear. Using syngeneic murine models, we integrated Nr4a3-Tocky reporter analysis with single-cell transcriptomics and T-cell receptor clonotyping comprehensively to profile intratumoural $CD8^+$ T-cells following RT/CRT. We show that CRT uniquely drives robust antigen-specific clonal expansion and biases differentiation toward progenitor (or precursor) exhausted (T_{PEX}) phenotypes, while RT favours terminal exhaustion (T_{EX}). Single-cell analyses reveal CRT-induced clonal dominance within T_{PEX} subsets, suggesting the potential for enhanced immune reinvigoration. In peripheral blood mononuclear cells (PBMCs) from patients treated with CRT, high levels of T_{EX} cells were found early and at 3 months post-treatment, with delayed peripheral T_{PEX} expansion at 3 months, indicating phased progenitor recovery. These findings demonstrate distinct immunological remodelling by CRT versus RT and underscore the critical importance of treatment timing for optimising combination immunotherapy strategies in LA-SCCHN.

INTRODUCTION

The interplay between tumour immunity and standard-of-care cancer therapeutics has become a major theme of oncological research. Central to this is the concept of the cancer-immunity cycle, a dynamic and potentially self-amplifying process through which tumour cell death fuels antigen release, dendritic cell (DC) activation, and subsequent T-cell priming, culminating in iterative cytotoxic responses against malignant cells (1). Yet, within the tumour microenvironment (TME), chronic antigen stimulation and immunosuppressive signals often derail T-cell differentiation, accelerating the emergence of dysfunctional, exhausted $CD8^+$ T-cell phenotypes (2). T-cell exhaustion, classically defined by impaired effector function and upregulation of inhibitory receptors such as PD-1, LAG-3, and TIM-3, represents a major barrier to durable tumour control (3). This state is generally seen as irreversible, particularly in the terminally exhausted (T_{EX}) subset. However, the less differentiated precursor exhausted (T_{PEX}) population, marked by the transcription factor TCF1, retains proliferative potential and responsiveness to immune checkpoint inhibitors (ICIs), positioning it as a key target for therapeutic approaches that seek to reinvigorate anti-tumour immunity (4-6).

While the spotlight in recent years has deservedly fallen on ICIs, an important paradigm shift has emerged: radiotherapy (RT) and chemoradiotherapy (CRT) – historically viewed as being immunosuppressive – can also profoundly modulate the immune landscape in an

immunostimulatory fashion. Indeed, clinical successes, such as the PACIFIC trial, illustrate the potential of RT and CRT to synergise with immunotherapy (7). RT and CRT can trigger immunogenic cell death (ICD), enhancing tumour antigen availability and inflammatory cytokine release (8). This process releases damage-associated molecular patterns (e.g., ATP, HMGB1, calreticulin), which activate both surface and intracellular pattern recognition receptors (PRRs) expressed by dendritic cells (DCs) and other antigen-presenting cells. These effects may transform the irradiated tumour into an *in-situ* vaccine capable of priming systemic, tumour-specific immune responses. Furthermore, recent studies have shown that CRT reshapes T-cell receptor (TCR) clonality by selectively expanding dominant T-cell clones associated with tumour specificity in head and neck, cervical, and rectal carcinomas (9-11). However, the functional consequences of this expansion remain unclear.

The incidence of squamous cell carcinoma of the head and neck (SCCHN) is rapidly rising in the developed world and it ranks as the seventh commonest cancer diagnosis worldwide (12). Definitive CRT remains standard-of-care for patients with unresected locally-advanced (LA) disease. Although the addition of cisplatin increases toxicity compared to RT alone, it improves local control and overall survival (13). The benefit of platin-based CRT is statistically significant and clinically meaningful, but relatively modest (approximately 6.5%) and only clearly apparent with meta-analysis of data from >100 trials (13). Attempts at de-escalation, through replacement of cisplatin with cetuximab, in HPV-associated oropharyngeal cancer have failed to reduce toxicity and have, instead, shown worse survival outcomes (14, 15), reinforcing the primacy of CRT as standard-of-care for unresected LA-SCCHN. Nonetheless, de-escalation strategies are still being investigated in select HPV-positive oropharyngeal cancer cohorts. For example, the ECOG-ACRIN 3311 trial showed that, in surgically resected intermediate-risk patients, adjuvant RT could be safely reduced from 60 Gy to 50 Gy without compromising disease control (16). In parallel, ^{18}F-fluoromisonidazole (FMISO) PET has been shown to identify hypoxia-negative tumours suitable for RT dose reduction, achieving excellent outcomes even with de-escalated CRT doses (~30 Gy), supporting its use as a potential functional biomarker to guide adaptive RT dose and volume reduction (17). Despite these advances in refining locoregional therapy, overall survival outcomes for patients with LA-SCCHN have plateaued, highlighting the need for novel strategies that move beyond optimisation of CRT parameters alone.

One promising avenue has been the integration of ICI with standard treatment backbones. However, the failure to improve outcomes by combining ICI directly with (C)RT, as evidenced in multiple phase III trials, such as JAVELIN Head and Neck 100 (18) , KEYNOTE-412 (19), GORTEC 2017-01 (20), IMvoke010 (21) and COMPARE (22), underscores a critical gap in

our understanding of how standard therapies shape the immune landscape. Preclinical models have almost exclusively focused on combining ICI with RT alone, failing to characterise potential differences in immunologic effects of CRT. While CRT is widely used and clinically effective, its immunomodulatory impact relative to RT, including how it influences T-cell differentiation trajectories, precursor exhaustion, and clonal dynamics, has largely been ignored. Notably, antigen persistence during CRT could promote both expansion and premature exhaustion of TILs, particularly in highly inflammatory environments like SCCHN (23). Emerging evidence underscores the prognostic and functional relevance of different $CD8^+$ T-cell exhaustion states in SCCHN. Higher frequencies of polyfunctional CD8+ T_{EX} were associated with improved overall and recurrence-free survival in one study (24), whereas another showed that $CD8^+$ T_{PEX} subset enrichment correlated with favourable outcomes (23). Transcriptional analyses implicate TCR signalling as a key determinant of exhausted T-cell responsiveness to neoadjuvant immunotherapy in SCCHN (25).

Therefore, we used syngeneic immunocompetent animal models to show that while both RT and CRT increase $CD8^+$ T-cell infiltration, only CRT depends on these cells for therapeutic efficacy. We show that CRT drives more focused clonal expansion and effector differentiation of antigen-engaged $CD8^+$ T-cells, with a preferential shift toward effector memory and T_{PEX}, rather than T_{EX}, states. Translational analyses of patient PBMCs revealed systemic immune modulation, with CRT associated with stronger T_{EX} accumulation and a delayed rise in putative T_{PEX} subsets compared with RT. Together, these findings define distinct immunologic consequences of RT and CRT, inform biomarker development, and provide a roadmap for rational integration of immunotherapy.

RESULTS

Radiotherapy (RT) and chemoradiotherapy (CRT) both increase $CD8^+$ T-cell infiltration into tumours, but the therapeutic effect is $CD8^+$ T-cell dependent only with CRT.

Compared to RT, CRT yielded a modest, non-significant improvement in tumour control in both mEER and MOC1 preclinical models (Fig. 1A, S1A, S2A), in line with the relatively modest benefits seen with meta-analysis in clinical studies (13). Survival was significantly prolonged in the mEER model (Fig. 1B), but not in MOC1 tumours (Fig. S2B). In the mEER model, $CD8^+$ tumour-infiltrating lymphocyte (TIL) dynamics varied over time following RT as determined by flow cytometry from baseline: numbers declined at day 3 post-RT, consistent with radiation-induced intratumoural lymphopenia, recovered by day 7 post-RT, and peaked at day 10 (Fig. 1C). Both RT and CRT increased $CD8^+$ TIL abundance compared to vehicle or

102 cisplatin-alone controls; however, no significant differences were observed between RT and
103 CRT at day 10 or day 14 following treatment when quantified by immunohistochemistry (Fig.
104 1D) and flow cytometry (Fig. 1E). Furthermore, there were no significant differences in the
105 percentage of PD-1^{hi} expressing CD8^{+} T-cells between RT and CRT treatment groups (Fig.
106 1F).

107 To assess the function of CD8^{+} T-cells, we performed depletion studies under RT and CRT
108 conditions. In the mEER model, RT-mediated tumour control was CD8^{+} T-cell-independent
109 (Fig. 1G, Fig. S1B), whereas CRT (cisplatin + RT) showed CD8^{+} T-cell-dependence, as
110 depletion significantly decreased tumour control (Fig. 1H, Fig. S1B, Fig. S3). These findings
111 indicate a mechanistic role for CD8^{+} T-cells in CRT response in this model. In the MOC1
112 model, which exhibits higher baseline CD8^{+} T-cell infiltration, depletion affected neither RT nor
113 CRT (Fig. S2D-E). Subsequent experiments focused on the mEER model, where CRT
114 conferred a modest survival benefit [in line with the clinical meta-analysis (13)], to investigate
115 how addition of cisplatin to RT modulates CD8^{+} T-cell function in this setting.

116 **CRT reduces the proportion of persistently engaged CD8^{+} TILs compared to RT.**

117 Immunoprofiling via flow cytometry of mEER tumours showed that RT and CRT broadly
118 enhanced lymphocyte activation, proliferation, and cytotoxicity, with CRT exerting the stronger
119 effect overall (Fig. S4). Both treatments increased CD44 expression (Fig. S4A) and expanded
120 granzyme B^{+}/perforin^{+} cytotoxic populations (Fig. S4B) across CD8^{+} T-cell, NK, and NKT
121 subsets. CRT significantly increased Ki67^{+} proliferating CD8^{+} T and NK cells (Fig. S4C), as
122 well as T-bet^{+} (Fig. S4D) expression in Tconv and CD8^{+} T-cells. Effector memory (Fig. S4E)
123 and PD-1^{+}/TIM-3^{+} checkpoint-positive (Fig. S4F) CD8^{+} T-cells were also increased by both
124 treatments.

125 As cisplatin-based CRT was CD8^{+} T-cell-dependent, whereas RT alone was not, we next
126 asked whether CRT differentially affects the quality or kinetics of T-cell antigen engagement
127 (Fig. 2A). To address this, we employed the Nr4a3-Tocky ("Timer of cell kinetics and activity"
128 reporter system) (26-28). This system utilises a Fluorescent Timer (FT) protein that undergoes
129 a spontaneous, time-dependent shift in Timer fluorescence following TCR-mediated induction
130 of Nr4a3, a TCR downstream nuclear receptor gene. The FT protein is initially expressed as
131 an immature blue fluorophore, which matures into a stable red fluorophore with a half-life of
132 approximately 4 hours (27). Consequently, newly antigen engaged T-cells express blue
133 fluorescence ("new"), persistently engaged T-cells express both blue and red ("persistent"),
134 and cells in which TCR signalling has ceased ("arrested") express red fluorescence only.

135 These dynamics are quantified using the 'Timer Angle', a trigonometric transformation where
136 0° (blue only) represents the onset of activation, 45° (blue and red) indicates sustained
137 persistent signaling, and 90° (red only) identifies the cessation of TCR engagement.
138 Additionally, the overall fluorescence intensity provides a qualitative measure of cumulative
139 TCR signal strength.

140 To evaluate treatment-induced remodeling of the immune landscape, UMAP analysis was
141 performed on concatenated $CD8^+$ TIL data from all treatment groups (Fig. 2B). Both
142 treatments increased the abundance of antigen-engaged, activated ($CD44^{hi}$ $CD69^{hi}$ $CD25^{hi}$)
143 and immune checkpoint-expressing ($PD\text{-}1^{hi}$ $TIM\text{-}3^{hi}$) $CD8^+$ TILs compared to vehicle or
144 cisplatin alone (Fig. 2C-F). This change was reflected in a significant increase in the frequency
145 of cluster 4 (Fig. 2C), which was predominantly composed of cells exhibiting high Timer
146 Intensity and 'persistent' TCR signal (Fig. 2D). Conversely, there was a corresponding
147 decrease in the frequency of clusters 2 and 5 (Fig. 2C), which were dominated by a profile of
148 timer-negative status, low activation and low immune checkpoint expression (Fig. 2D-F).

149 Focusing on the comparison between RT and CRT, a notable difference emerged within
150 cluster 3. CRT-treated tumours exhibited a significant decrease in this cluster (Fig. 2C), which
151 was defined by a "persistent-arrested" antigen engagement profile – characterised by
152 sustained TCR signalling – despite displaying activation and immune checkpoint marker
153 expression comparable to cluster 4 (Fig. 2D-F). Overall, CRT did not enhance overall antigen
154 engagement compared to RT but, instead, specifically reduced the proportion of "persistent-
155 arrested" (PAt) $CD8^+$ TILs relative to vehicle controls (Fig. 2G). This subset may represent
156 terminally exhausted cells, secondary to continuous antigen engagement (3, 29, 30).

157 Interestingly, addition of anti-PD-1 antibody (αPD-1) had no effect with RT alone (Fig. S5A),
158 while there was a modest, but statistically non-significant, improvement in tumour control with
159 αPD-1 in CRT-treated mice (Fig. S5B). These findings suggest differential impacts of RT and
160 CRT on T cell exhaustion, motivating further interrogation of the transcriptional and phenotypic
161 states of antigen-engaged TILs using single-cell approaches.

162 **CRT increases antigen-engaged TILs with effector memory (T_{EM}) relative to naïve**
163 **phenotype (T_N), when compared to RT alone.**

164 To investigate the impact of CRT on T-cell phenotypes in more detail, we combined the Nr4a3-
165 Tocky system with single-cell transcriptomic and protein profiling, using AbSeq, and TCR
166 sequencing (Fig. 3A). Tumours and tumour-draining lymph nodes (TDLNs) were harvested

167 from mice treated with vehicle, RT, or CRT, and cells were analysed by UMAP clustering
168 based on AbSeq expression profiles (Table S3). Within the tumour, TILs were dominated by
169 effector memory (T_{EM}) phenotype (CD62L$^-$ CD44$^+$), whereas T-cells from TDLNs were
170 primarily naïve (T_N; CD62L$^+$) and central memory (T_{CM}; CD62L$^+$, CD44$^+$) (Fig. 3B-E).

171 Within TILs, following both RT and CRT, there was increased expression of activation markers
172 (CD69, CD38), co-stimulatory receptors (CD278 [ICOS], CD137 [4-1BB]) and markers of
173 inhibition/exhaustion (CD223 [LAG3], CD366 [TIM-3]), TIGIT and NKG2A-C-E) compared to
174 vehicle. There was also a reduction in the average expression of the activation/Treg marker,
175 CD25 compared to vehicle (Fig. 3F). Again, focusing particularly on differences with the
176 addition of chemotherapy to RT, compared to RT alone, CRT showed increased KLRG1,
177 CD278 (ICOS), CD28 and CD244a expression and reduced CD27 and CD38 expression. This
178 profile is consistent with chemotherapy enhancing the induction of T_{EM} relative to naïve T-
179 cells, compared to RT alone.

180 **Persistently-engaged T-cells express higher levels of multiple inhibitory checkpoint**
181 **molecules consistent with continual antigen engagement driving T-cells towards**
182 **exhaustion**.

183 To assess the temporal dynamics of antigen engagement across treatment groups, we
184 mapped Tocky-defined populations ("persistent" [pers], "arrested" [arr], and "timer-negative"
185 [neg]) onto the UMAP landscape (Fig. 3G). Untreated tumours (Tum_Veh) exhibited sparse
186 antigen-engaged T cells, with a predominance of timer-negative cells. In contrast, both RT
187 and CRT markedly induced a striking predominance of antigen-engaged TILs within the TME.
188 This expansion was most pronounced following CRT, which demonstrated a dense and
189 cohesive accumulation of "persistent" (pers) T-cells (purple in Fig. 3G), indicative of sustained
190 TCR signalling.

191 Examination of marker expression across Tocky populations showed that "persistent" T-cells
192 expressed markedly higher levels of multiple immune checkpoint markers: CD279 (PD-1),
193 CD233 (LAG-3), CD366 (TIM-3) and TIGIT, and the exhaustion-associated markers, CD244a
194 and NKG2A-C-E, compared with other Tocky loci (Fig. 3H). This profile is consistent with
195 continual antigen engagement driving T-cells towards an exhausted phenotype (3). In
196 contrast, "timer-negative" T-cells demonstrated relatively higher expression of CD62L, CD103,
197 CD27 and CD28, indicative of a less antigen-experienced or memory-associated state (Fig.
198 3H). Interestingly, while the "arrested" Tocky population displayed intermediate levels of
199 immune checkpoints (e.g. PD-1, LAG-3, TIM-3), they reached a positive peak in CD69

200 expression and a negative peak in CD27. Furthermore, the inclusion of KLRG1-high cells
201 within the arrested population suggests that these cells sustain enhanced cytotoxic potential
202 (Fig. 3H). These dynamics suggest that T-cells with historical antigen engagement undergo
203 an active remodelling phase at the Arrested stage, leaving the terminal exhaustion state
204 observed in persistently stimulated cells.

205 While the single-cell transcriptomic analysis demonstrates increased overall antigen
206 engagement following CRT, the persistent-arrested (PAt) subset defined by Nr4a3-Tocky
207 dynamics cannot be directly identified within the scRNA-seq dataset (Fig. 3G). However, flow
208 cytometry using the Tocky reporter revealed that CRT reduced the proportion of PAt cells
209 compared with RT alone (Fig. 2G). Together, these findings indicate that CRT is associated
210 with increased overall T-cell antigen engagement while reducing the accumulation of more
211 exhausted PAt cells, relative to RT alone.

212 **CRT leads to more focused, clonally expanded CD8$^+$ T-cell populations with an effector**
213 **profile.**

214 Clonal expansion occurred almost exclusively within tumours treated with RT and CRT, with
215 CRT leading to greater clonal expansion than RT alone (Fig. 4A-D). Interestingly,
216 hyperexpanded clones were made up of only three paired TCR α/β CDR3 sequences, that
217 occurred exclusively in T-cells from tumours treated with CRT, highlighting striking clonal
218 dominance (Fig. 4B). Following downsampling to the minimum clonotype count for
219 comparability, consistently lower diversity in TILs from CRT- versus RT-treated tumours was
220 still found by various indices (Fig 4E). For reference, Shannon and Simpson indices combine
221 clonotype richness and evenness, Chao1 and ACE indices estimate unseen diversity and the
222 Inverse Pielou index was used to assess clonal skewing (31). Hence, the TCR repertoire in
223 the CRT group was less even than RT and more clonal/skewed towards dominant clones.
224 With increasing clonal expansion, a progressive predominance of CD8$^+$ over CD4$^+$ T-cells was
225 observed, with hyperexpansion occurring exclusively within the CD8$^+$ compartment (Fig. 4F).

226 Hence, CRT reshaped the TCR repertoire of TILs and altered the expression profile of
227 hyperexpanded CD8$^+$ T-cells. In all singleton clones across treatment conditions, there was a
228 predominance of naïve or early memory (CD44^{lo}, CD62L^{hi}, CD27^{hi}, CD28^{hi}) and/or tissue-
229 resident T-cells (CD103^{hi}) (Fig. 4G). When the expression profile of the hyperexpanded clones
230 (seen only with CRT) was examined, relatively higher expression of the activation marker
231 CD44 was observed, with relatively lower multiple immune-checkpoint /inhibitory markers –
232 CD279 (PD-1), CD223 (LAG-3), TIGIT and CD38, compared to the other clonal subgroups

233 (Fig. 4G). These findings suggest that CRT-induced hyperexpanded CD8$^+$ T-cells
234 predominately acquire an effector-like, rather than exhausted, phenotype.

235 **CRT leads to greater clonal expansion of antigen-engaged CD8$^+$ T-cells than RT.**

236 Correlation of TCR-seq data with the Tocky profile revealed that CRT induced greater clonal
237 expansion of antigen-engaged tumour-infiltrating CD8$^+$ T cells ("persistent" and "arrested")
238 compared to RT, whereas vehicle-treated tumours showed minimal clonal expansion (Fig. 5A–
239 B). In contrast, TILs lacking evidence of antigen engagement at the time of analysis ("timer-
240 negative") demonstrated limited clonal expansion across treatment groups.

241 Given that Timer fluorescence reflects real-time TCR signalling dynamics, the enrichment of
242 expanded clonotypes within the "persistent" compartment in CRT-treated tumours (Fig. 5B)
243 suggests that a discrete subset of clones is either undergoing sustained proliferative
244 expansion driven by continuous antigen stimulation or, alternatively, that once expanded,
245 these clones preferentially occupy and remain within the persistently engaged niche.

246 Despite treatment-matched sampling, we observed limited clonal overlap between tumour and
247 TDLN compartments (Fig. S6). Together with the apparent confinement of expanded
248 clonotypes to defined Tocky signalling stages (Fig. 5B, S7), this supports a model in which
249 CRT promotes spatially restricted, antigen-dependent clonal expansion within the TME.

250 **Clonal CD8$^+$ TILs treated with CRT show relative acquisition of a less exhausted**
251 **phenotype as they progress from "persistent" to "arrested".**

252 To capture broader antigen-driven activity, the expression profile of specific clonal populations
253 (frequency ≥5) was studied in relation to their Tocky profile in different samples. Firstly, clonal
254 "persistent" CD8$^+$ TILs were compared between tumours treated with RT and CRT; CD8$^+$ TILs
255 from CRT-treated tumours showed increased expression of activation and co-stimulation
256 markers (CD44, CD28 and CD154 [CD40L]), the residency marker CD103, and antigen-
257 experienced/ exhaustion markers (CD244a, PD-1, CD366 [TIM-3], NKG2A-C-E), as compared
258 to RT-treated tumours (Fig. 5C). Overall, this suggests that continuously antigen-engaged
259 CD8$^+$ TILs shift towards a more activated, tissue-resident, and partially exhausted phenotype
260 following CRT, rather than RT.

261 Next, all clonal CD8$^+$ TILs with a frequency ≥5 from CRT-treated tumours were examined by
262 Tocky profile; these were "persistent" versus "arrested", as there were no sufficiently expanded

263 cells in the “new” or “timer negative” subsets (Fig. 5D). Here again, consistent with the model
264 of chronic antigen stimulation driving exhaustion, persistently antigen-engaged $CD8^+$ TILs
265 exhibited reduced activation (CD44) and increased expression of multiple immune
266 checkpoints, CD279 (PD-1), CD223 (LAG-3), CD366 (TIM-3) and TIGIT, compared to
267 historically antigen-engaged, but now “arrested”, cells. Moreover, a small percentage of
268 “persistent” cells showed elevated levels of the terminal differentiation marker KLRG1
269 compared to “arrested”. Collectively, these findings suggest that progression along the Tocky
270 trajectory from “persistent” to “arrested”, rather than sustained antigen re-engagement to
271 maintain the “persistent” state, may mitigate T-cell exhaustion. Of note, this analysis could not
272 be performed for TILs from RT-treated tumours, as there were no “arrested” clonal (frequency
273 ≥5) $CD8^+$ TILs present in this subset, only “persistent” cells.

274 Clonal $CD4^+$ TILs, with a frequency ≥5, were only present in tumours treated with CRT and
275 not RT (Fig. 5E). This is consistent with a model in which $CD4^+$ T-cells support enhanced
276 clonal expansion of $CD8^+$ TILs following CRT more effectively than after RT alone. Similarities
277 were observed in the expression profiles of “persistent” and “arrested” clonal $CD4^+$ and $CD8^+$
278 TILs; for example, “persistent” $CD4^+$ TILs also exhibited higher expression of
279 inhibitory/exhaustion-associated markers such as LAG3 and KLRG1, as well as activation
280 markers CD25 and CD137 (4-1BB), compared to their “arrested” counterparts (Fig 5D-E).
281 These are consistent with “persistent” cells representing a more chronically stimulated and
282 potentially exhausted state in both $CD4^+$ and $CD8^+$ TILs.

283 **CRT compared to RT increases the proportion and clonal expansion of precursor**
284 **exhausted (T_{PEX}), relative to terminally exhausted (T_{EX}), CD8+ TILs in the arrested phase.**

285 To define treatment-induced changes in T-cell states, sorted single T-cells were subjected to
286 UMAP clustering based on their global transcriptomic profiles. Due to inadequate cell numbers
287 and integrity, scRNAseq data was only available for “arrested” (arr) and “timer negative” (neg)
288 samples, which nevertheless reflect either end of the Timer expression trajectory. UMAP
289 clustering initially identified 11 transcriptionally distinct T-cell clusters. Based on shared
290 lineage markers, characteristic gene expression of T_{PEX} and T_{EX} states in the published
291 literature (4, 6, 32), and proximity in low-dimensional space, closely related clusters were
292 consolidated into 9 annotated T-cell subsets.

293 As shown in Fig. 6A-B, naïve $CD4^+$ and $CD8^+$ T-cells were identified by high expression of
294 CD62L (*Sell*). Classical $CD8^+$ T_{PEX} cells were characterized by elevated TCF1 (*Tcf7*),
295 intermediate PD-1 (*Pdcd1*), and low TIM-3 (*Havcr2*) and CD62L (*Sell*), indicative of antigen

experience with preserved progenitor features (4, 6, 32). CD8$^+$ T_{EX} cells expressed low TCF1, but high TOX, PD-1, LAG-3, and TIM-3, with interestingly maintained Granzyme B (*Gzmb*) and perforin (*Prf1*) expression expression. CD8$^+$ cytotoxic ("cyto") cells exhibited high expression of granzymes (*Gzma, Gzmb*) and perforin (*Prf1*), not falling into the T_{PEX} or T_{EX} phenotype. Two distinct FOXP3-enriched Treg-like subsets were identified: Treg1, displaying an effector/suppressive phenotype (high PD-1, CTLA-4, ICOS, IL2RB and ID2), and Treg2, with a more naïve/central-memory profile (high CD62L and IL7R). Both states correspond to previously described functional Treg phenotypes documented in regulatory T-cell heterogeneity studies (33, 34).

Consistent with AbSeq profiling, TILs were enriched for antigen-experienced populations, including CD8$^+$ T_{PEX}, CD8$^+$ T_{EX}, and Treg1 (Fig. 6C), whereas TDLNs were dominated by naïve CD8$^+$ T-cells and Treg2 (Fig. 6D). Within the arrested TILs compartment, both RT and CRT increased the frequency of CD8$^+$ T_{EX} compared to vehicle, with RT inducing a larger increase. Conversely, CRT preferentially expanded CD8$^+$ T_{PEX} compared to RT (Fig. 6C). In the timer-negative compartment, both RT and CRT similarly enhanced the proportion of T_{PEX} and T_{EX} compared to vehicle. These findings suggest that, in cells with a history of antigen engagement, CRT skews differentiation toward progenitor-like states, while RT promotes more terminal T-cell exhaustion.

To explore transcriptional clonal dynamics, we integrated paired TCR VDJ and scRNA-seq profiles, mapping clonotypes onto UMAP-defined subsets (Fig. 6E). In total, 78.2% (1,410/1,803) of arrested and 81.8% (1,084/1,325) of timer-negative T-cells were clonotyped. Clonal expansion occurred mainly in "arrested" TILs rather than T-cells from TDLNs (Fig. S8). As shown in Fig. 6F, large and hyperexpanded clones were exclusively observed in CRT-treated TILs, predominantly within CD8$^+$ T_{PEX} and, to a lesser extent, CD8$^+$ T_{EX} and Treg1 subsets. Notably, the majority of hyperexpanded clones resided in the T_{PEX} population, whereas RT-induced expansion was restricted to smaller clones within T_{EX} clusters (Fig. 6G). Thus, CRT promotes robust clonal expansion of T_{PEX} cells, while RT favours expansion of terminally exhausted subsets. However, the presence of clonally expanded Treg1 population may contribute to an inhibitory TME, that limits the functional reinvigoration of CD8$^+$ T-cells with anti-PD-1 (Fig. S5), despite CRT-induced expansion of T_{PEX} populations.

Overall, compared to vehicle, CRT reduced the proportion of T_{EX} CD8$^+$ TILs and increased T_{PEX} populations, whereas RT drove the opposite trend. These results, supported by lineage and clonotype mapping, indicate that CRT preferentially maintains and/or expands progenitor-exhausted states, potentially preserving anti-tumour functionality compared to RT alone.

330 **Enhanced T-cell activation and altered exhaustion dynamics after CRT versus RT in**
331 **human PBMCs**

332 To provide proof-of-concept translational validation of CRT's impact on the T-cell exhaustion
333 trajectory versus RT, we analysed a small exploratory cohort of patients with LA-SCCHN
334 receiving definitive RT (n=4) or CRT (n=8) as part of the INOVATE study (ISRCTN32335415).
335 Peripheral blood mononuclear cells (PBMCs) were collected from patients receiving RT or
336 CRT at baseline, week 3 of RT (RTW3), and 3 months post-treatment (RTFU), and analysed
337 by flow cytometry. Over time, there was a trend toward a reduction in $CD4^+$ Tconv and an
338 increase in $CD8^+$ T-cell frequencies related to $CD45^+$ population, more pronounced in CRT
339 than RT (Fig. 7A). At the 3-month follow-up, only CRT induced a significant fold change in
340 $CD8^+$ T-cells relative to baseline (Fig. 7B). CRT was also associated with increased Granzyme
341 B^+ $CD8^+$ T-cells and $CD56^+$ NK-like $CD4^+$ Tconv (35-37) at follow-up, indicative of enhanced
342 cytotoxic activity (Fig. 7C). In parallel, proliferating $Ki67^+$ Treg were significantly reduced after
343 CRT but not RT (Fig. 7D), while PD-1 expression on both $CD4^+$ Tconv and $CD8^+$ T-cells was
344 increased after CRT (Fig. 7E). Examination of exhaustion marker trajectories revealed that
345 both RT and CRT showed trends toward increasing putative T_{EX} $CD8^+$ T-cells (TOX^+ $TCF\text{-}1^-$
346 $PD\text{-}1^{hi}$) (38-40) during treatment (Fig. 7F). Notably, a significant increase in putative T_{PEX} cells
347 ($TCF\text{-}1^+$ TOX^- $PD\text{-}1^{int}$) (5, 40, 41) emerged only after CRT at the 3-month follow-up (Fig. 7F).
348 Hence, even with this limited number of patients, these data revealed longitudinal differences
349 between RT and CRT in peripheral T-cell subset composition, cytotoxic activity, and
350 exhaustion trajectories that mirror the data generated in the mouse model.

351 **DISCUSSION**

352 This study demonstrates that chemoradiotherapy (CRT) reshapes the intratumoural T-cell
353 immunological landscape more favourably than radiotherapy (RT) alone in a relevant SCCHN
354 tumour model (Fig S9). Functional $CD8^+$ T-cell depletion experiments confirmed that tumour
355 control under CRT, but not RT, depends on $CD8^+$ T-cells, establishing their essential role in
356 mediating CRT efficacy. Using the Nr4a3-Tocky reporter system combined with single-cell and
357 clonotype analyses, we show that CRT enhances antigen engagement, promotes robust
358 clonal expansion of $CD8^+$ tumour-infiltrating lymphocytes (TILs), and biases differentiation
359 toward a progenitor exhausted (T_{PEX}), rather than terminally exhausted (T_{EX}), fate. These
360 immunological effects may be driven by the additive benefits of chemotherapy-induced
361 immunogenic cell death and RT-mediated antigen release, which collectively broaden tumour
362 antigen availability.

363 Both RT and CRT increased TIL activation and immune checkpoint expression; however, CRT
364 induced a more clonally-focused $CD8^+$ T-cell repertoire, including hyperexpanded clones,
365 made up of only three paired TCR α/β CDR3 sequences (Fig. 4B), not observed with RT.
366 These dominant clonotypes exhibited an effector-like phenotype with high CD44 and lower
367 expression of inhibitory receptors (PD-1, LAG-3, TIGIT, CD38), suggesting functional
368 persistence rather than terminal exhaustion. In contrast, RT-driven expansion was limited and
369 enriched in T_{EX} subsets, a population associated with poor reinvigoration capacity. These
370 observations are consistent with prior studies implicating T_{PEX} cells as key mediators of
371 durable antitumour immunity and checkpoint blockade responsiveness (4, 6, 32).

372 Single-cell transcriptomics confirmed distinct T_{EX} and T_{PEX} states within TILs and revealed
373 treatment-specific patterns. CRT enriched for T_{PEX} cells characterised by high *Tcf7*,
374 intermediate *Pdcd1*, and low *Havcr2* expression, while RT promoted T_{EX} accumulation.
375 Integration of clonotype and phenotype mapping revealed that large-to-hyperexpanded clones
376 were restricted to CRT-treated tumours, primarily within T_{PEX} clusters, whereas RT-induced
377 clonal expansion was sparse and largely confined to T_{EX} cells. These findings suggest that
378 CRT not only broadens antigen engagement but also sustains clonal persistence in a less
379 exhausted state, which may support combination immunotherapy. However, CRT clonally
380 expanded Treg1, a Treg-like subset, with a suppressive transcriptional profile characterised
381 by high PD-1, CTLA-4, ICOS, IL2RB, and ID2 expression which could counterbalance effector
382 gains by limiting the functional reinvigoration of $CD8^+$ T-cells. This may explain the limited
383 clinical benefit of PD-1 blockade in this setting (consistent with our pre-clinical model data
384 shown in Fig. S5), highlighting the need for additional combination strategies targeting
385 regulatory populations such as anti-CD25 therapy. Interestingly, no shared clonotypes were
386 detected between TDLNs and tumours, possibly due to limited sequencing depth, pooled
387 sampling across animals, or the timing of tissue collection. However, shared clonotypes along
388 the Tocky trajectory within TILs support antigen engagement as a driving force for clonal
389 expansion within tumours.

390 From a translational perspective, these findings underscore the immunomodulatory potential
391 of CRT beyond local tumour control. By preserving a pool of progenitor-like $CD8^+$ T-cells and
392 limiting terminal exhaustion, CRT may create a TME more able to contribute to systemic
393 immune surveillance and amenable to reinvigoration by ICIs. Human PBMC analyses
394 revealed that CRT induced persistently high putative T_{EX} $CD8^+$ T-cells during treatment (week
395 3) and at 3 months post-treatment, while a significant increase in putative T_{PEX} cells emerged
396 only at the later 3-month timepoint, and this was seen with CRT treatment only. This delayed
397 T_{PEX} expansion may represent a recovery phase critical for effective antitumor immunity and

398 responsiveness to ICIs. Concurrently, CRT was associated with increased cytotoxic potential,
399 including higher Granzyme B$^+$ CD8$^+$ T-cells and CD56$^+$ Tconv, as well as reduced proliferating
400 Tregs, suggesting a shift toward a more active, systemic anti-tumour immune milieu. These
401 data suggest that CRT modulates systemic lymphocyte immunity more favourably than RT
402 during and after treatment. Importantly, these observations are supported by our group's prior
403 TCR sequencing work, which demonstrated that CRT promotes maintenance and expansion
404 of pre-existing peripheral T-cell clonotypes associated with treatment response (9). However,
405 as our analyses were performed in peripheral blood rather than tumour tissue, they fail to
406 capture fully the intratumoral immune dynamics observed in our preclinical mouse models.
407 The early and persistent dominance of systemic T_{EX} cells may also limit effective reinvigoration
408 of T_{PEX} cells by PD-1-targeted therapies. These findings align with clinical trial data showing
409 disappointing outcomes when ICIs are given concurrently with CRT in unresected LA-SCCHN
410 (18-20). Our results highlight the importance of carefully timing ICI relative to CRT to capitalise
411 on the potential window of progenitor T-cell expansion and improve therapeutic synergy.

412 Limitations of this study include modest single-cell RNA sequencing depth, which restricted
413 the resolution of low-abundance transcripts and trajectory analysis. The exclusive analysis of
414 sorted T-cells prevented broader immune cell interactions within the TME from being captured.
415 Additionally, pooled tumour and TDLN samples from multiple mice may have masked
416 individual-level clonal overlaps. The small number of patients in the translational cohort is also
417 a limitation of this work. Future studies with longitudinal tumour sampling – both in preclinical
418 models and from patients – together with deeper sequencing and paired tumour-TDLN
419 analyses, could better clarify the dynamics of priming, trafficking, and differentiation in this
420 setting.

421 Future clinical strategies should consider sequencing and biomarker-driven timing of
422 immunotherapy. Rational combinatorial treatment strategies, that move beyond immune
423 checkpoint inhibition (ICI) alone with CRT, could include Treg depletion (e.g. anti-CD25
424 antibodies) (42), targeting immunosuppressive myeloid populations (43), or radio-sensitising
425 agents that enhance immunogenic cell death to further amplify antigen release and CD8$^+$ T-
426 cell priming (44). Such approaches may provide the additional immune support required to
427 translate CRT-ICI synergy into meaningful clinical benefit.

428 In conclusion, our data demonstrate that the benefit of adding chemotherapy to radiotherapy
429 extends beyond direct radiosensitisation of tumour cells. CRT remodels the TIL compartment
430 by expanding antigen-engaged CD8$^+$ T-cells, promoting clonal dominance, and sustaining
431 progenitor-like states linked to durable antitumour immunity. These mechanistic insights into

432 the T_{PEX}/T_{EX} exhaustion trajectory provide a rationale for optimising the timing of CRT-based
433 immunotherapy regimens in SCCHN, with future work focused on refining combination
434 strategies that overcome residual immunosuppressive barriers.

435 **METHODS**

436 **Mouse models of head and neck cancer**

437 All procedures involving animals were approved by the Animal Ethics Committee at The
438 Institute of Cancer Research in accordance with National Home Office Regulations under the
439 Animals (Scientific Procedures) Act 1986. Wild-type or Nr4a3-Tocky C57BL/6 female mice (8-
440 14 weeks) were housed under specific pathogen-free conditions with ad libitum food and
441 water. The HPV-positive syngeneic mouse SCCHN mEER cell line was a gift from Dr Paola
442 Vermeer (Sanford Research, USA) and HPV-negative C57BL/6 carcinogen-induced mouse
443 oral cancer cell line MOC1 (45) were kindly provided by Ravindra Uppaluri (Dana-Farber
444 Cancer Institute). Cells were cultured in complete DMEM (Gibco) supplemented with heat-
445 inactivated 5/10% FBS, 1% L-glutamine and 0.5% penicillin-streptomycin. 1×10^6 mEER cells
446 or 4×10^6 MOC1 cells were injected subcutaneously into the right flank under isoflurane
447 anaesthesia. Tumour and weight measurements were taken twice weekly using calipers by
448 an independent animal technician. Tumour volume (mm^3) was calculated as length $\times$ width $\times$
449 height $\times$ 0.5236. For all studies, mice were randomised prior to treatment initiation for
450 comparable tumour volumes between cohorts. Euthanasia was performed via cervical neck
451 dislocation upon reaching humane endpoints, which included a maximum tumour diameter of
452 15 mm, $\geq$18% loss of body weight from peak weight, or clinical signs of distress.

453 ***In vivo* treatments**

454 *In vivo* treatments were commenced at 14-18 days post-implantation for mEER or 28-35 days
455 for MOC1, when tumour volumes reached approximately 30-60 mm^3. For radiotherapy (RT),
456 mice were anaesthetized with ketamine/xylazine and positioned prone under lead shielding
457 with a 16 mm aperture over the tumour. mEER tumours received 8 Gy × 3 fractions and MOC1
458 tumours 6 Gy × 3 fractions on alternate days using an AGO 250 kV X-ray unit (dose rate:
459 1.62 Gy/min). Dosimetry was verified using a calibrated Farmer Chamber and Unidos-E
460 Dosimeter (both PTW).

461 For chemoradiotherapy (CRT), cisplatin (7 mg/kg) was administered intraperitoneally 1 h
462 before each RT fraction. Where indicated, immune checkpoint blockade was delivered via

463 intraperitoneal anti–PD-1 (200 µg, clone RMP1-14) or isotype control twice weekly for up to
464 six doses. $CD8^+$ T-cell depletion was performed using anti-CD8α antibody (loading dose
465 400 µg, maintenance 200 µg twice weekly) or isotype control. Cisplatin (7 mg/kg) was
466 administered by i.p. injection one hour prior to RT (if delivered). Where indicated, anti-PD-1
467 (200 µg, clone: RMP1-14, BioXCell) or rat IgG2a isotype control (clone: 2A3, BioXCell) were
468 administered by i.p. injection twice-weekly for up to six doses. $CD8^+$ T-cell depletion was
469 performed using an anti-CD8α antibody (loading dose 400 µg, maintenance 200 µg twice
470 weekly; clone: 2.43, BioXCell) or rat IgG2b isotype control (clone: 1-2, BioXCell) for up to 10
471 doses. Confirmation of *in vivo* $CD8^+$ T-cell depletion using this regimen is outlined in Fig. S3.

472 **Histopathology**

473 Mouse specimens were fixed in 10% neutral buffered formalin (Sigma-Aldrich, HT501128) for
474 24 hours at room temperature, after which they were transferred to PBS at 4˚C. Paraffin
475 embedding of fixed material and immunohistochemistry (IHC) staining was performed by the
476 ICR Histopathology Core Facility. Anti-CD8α (Abcam, clone: EPR21769) was used with heat
477 induced epitope retrieval using Agilent Target Retrieval solution pH9 and Agilent rabbit
478 EnVision reagent as the detection system. Slides were scanned and imaged using
479 Hamamatsu Nanozoomer (Hamamatsu Photonics). Positive cell detection analysis on IHC
480 slides was performed using QuPath v0.5.1.

481 **Flow cytometry analysis**

482 Harvested mouse tumours were dissociated mechanically using scissors and enzymatically
483 digested in PBS containing 0.5 mg/mL collagenase type 76 I-S (Sigma-Aldrich), 0.4 mg/mL
484 Dispase II protease (Sigma-Aldrich), 0.2 mg/mL DNase I (Roche) and 4% Trypsin. Following
485 digestion, samples were passed through a 70 µm cell strainer and washed with FACS buffer
486 (PBS/2% FBS/5 mM EDTA). Lymph nodes were made into a single-cell suspension by
487 passage through a 70 µm cell strainer. For some experiments, mice were bled 10-20 µL from
488 the tail vein, and red blood cell lysis was performed by incubation in ACK lysis buffer (Thermo
489 Fisher Scientific) for 2 min. Human cryopreserved PBMCs were thawed using CTL Anti-
490 Aggregate Wash Supplement (Cellular Technology Limited) according to the manufacturer's
491 protocol. Samples were centrifuged at 300 g for 5 min at 4°C, washed and resuspended in
492 FACS buffer for Fc blocking and staining. Cells were incubated 4 °C for 10 min with anti-
493 mouse (BD Pharmingen) or anti-human CD16/CD32 (BD Pharmingen) prior to surface
494 staining, 4 °C for 30 min. Dead cells were excluded by using the Fixable Viability Dye eFluor
495 780 (Thermo Fisher Scientific) and the complete list of antibodies used for staining in this

496 study is provided in Table S1-S2. Intracellular staining was performed using the
497 Foxp3/Transcription Factor Staining Buffer Set (Thermo Fisher Scientific) as per
498 manufacturer's protocol. All samples were acquired on a BD FACSymphony A5 Cell Analyser.
499 Flow cytometry data was analysed using the FlowJo software (v10) and Tocky timer data was
500 analysed using the "TockyAnalysis" package in R (v3.6.3). Gating strategies for different
501 immune cell populations are detailed in Supplementary information (Fig. S10-S13).

502 **Single-cell RNA/TCR/Abseq profiling**

503 Tumours and TDLNs from mEER tumour-bearing Nr4a3-Tocky mice were collected 10 days
504 following the final dose of RT. Mice (n=12 per treatment group) received vehicle, RT, or CRT
505 on day 14 post-tumour inoculation; one wild-type mouse was included for gating control.
506 Tumours and TDLN were processed to form single-cell suspensions and pooled by treatment
507 group and tissue type, generating six pooled samples. For tumour samples, samples were
508 filtered and enriched for $CD45^+$ cells with mouse CD45 (TIL) microbeads (Milentyi Biotec)
509 according to manufacturer's protocol with LS columns on the QuadroMACS magnet (Milentyi
510 Biotec). Following this, cells were stained with AbSeq oligonucleotide-conjugated antibodies
511 (Table S3) and sample tags for cellular indexing of transcriptomes and epitopes by sequencing
512 (CITE-seq). Following flow cytometry staining, live $TCR\beta^+$ cells were sorted into four Tocky-
513 defined populations ("new," "persistent," "arrested," and "timer-negative") using a BD
514 FACSymphony S6 cell sorter, sorting strategies as detailed in Fig. S14. Sorted populations
515 were processed on the BD Rhapsody system for single-cell capture, cDNA synthesis, and
516 library preparation following the manufacturer's protocol. Libraries for whole-transcriptome
517 analysis (WTA), AbSeq, Sample Tags, and TCR sequencing were prepared and sequenced
518 on Illumina NovaSeq platforms. Additive results from three sequencing runs (repeated due to
519 technical issues), resulted in RNA libraries sequenced to a mean depth of 8,016 reads and
520 2,644 molecules per cell; AbSeq libraries reached a mean of 8,552 reads and 3,098 molecules
521 per cell; and TCR libraries achieved a mean of 2,396 reads and 6.35 molecules per cell. Raw
522 data was aligned and pre-processed using the BD Rhapsody pipeline and further filtered to
523 retain cells with ≥10 detected proteins, ≥500 AbSeq unique molecular identifiers (UMIs), and
524 mitochondrial content <20%. After quality control, at least 3,600 cells were retained in each of
525 the "persistent", "arrested", and "timer-negative" populations. In contrast, relatively few "new"
526 Tocky cells (~200) passed QC, which limits the interpretability of analyses within this subset.
527 Downstream analyses were performed in R (v4.3.3).

528

529 **Bulk RNA and TCR sequencing**

530 Mouse tumours were harvested 14 days after the last radiation dose and snap frozen on dry
531 ice. Tumour tissue was homogenised in 1 mL of Buffer RLT Plus (Qiagen) with 10 µL β-
532 mercaptoethanol (Gibco) within CK28 hard tissue homogenising 2 mL tubes (Precellys) using
533 the Precellys Evolution Homogeniser. RNA was extracted tumours using the RNeasy Plus
534 Mini Kit with QIAshredder (Qiagen) according to manufacturer's protocol. Library preparation
535 and sequencing were performed by Genewiz, Germany. Library preparation was strand-
536 specific with polyA selection, with 2×150bp sequencing at 20 million paired-end reads per
537 sample performed on an Illumina NovaSeq. Salmon quant v1.10.1 (46) was used for
538 transcript-level quantification against the GRCm39 mouse reference (Ensembl release 103).
539 Transcript-level abundance estimates were aggregated to gene-level using tximport v1.34 R
540 package (47). Differential gene expression analysis was performed using DESeq2 (48)
541 (pseudogenes were excluded and only genes with more than 10 reads in at least 5 samples
542 were kept in the analysis). Cell type signature genes were obtained from single-cell RNA
543 sequencing data from oropharyngeal squamous cell carcinoma patients (49) and signature
544 scores were calculated using the GSVA package (v2.0.4) (50) applied to counts normalised
545 using variance stabilising transformation. Gene set enrichment analysis was performed using
546 the clusterProfiler package (v4.14.4) (51).

547 **Human studies**

548 Peripheral blood was collected from patients with LA-SCCHN treated with definitive RT (n=4)
549 or CRT (n=8) as part of the INOVATE study (Investigation of Novel Plasma Human Papilloma
550 Virus DNA Assay for Treatment Response Estimation in Head and Neck Cancer,
551 ISRCTN32335415). All patients were aged ≥18 years with newly diagnosed HPV p16-positive
552 T1-T2/N1-3 or T3-T4/N0-3 squamous cell carcinoma of the oropharynx undergoing radical
553 treatment with RT or CRT. Samples were collected at baseline, week 3 of RT (RTW3), and at
554 3 months post-treatment (RTFU); one patient in the RT cohort had a follow-up collection at 6
555 weeks due to scheduling constraints. PBMCs were isolated using a density gradient medium
556 (Lymphoprep, STEMCELL Technologies) and stored in liquid nitrogen until analysis.

557 **Statistical analysis**

558 Statistical analyses were performed using GraphPad Prism version 10. Data are presented as
559 means ± SEM and are derived from single or pooled results of two to three independent
560 experiments. Area under the curve (AUC) was used to compare tumour growth between

561 groups. Survival differences were assessed using the log-rank (Mantel-Cox) test. Parametric
562 tests were applied only to data with normal distribution, confirmed via the Shapiro–Wilk test.
563 For comparisons between two groups, either a two-tailed unpaired t-test or Mann–Whitney U
564 test, or Wilcoxon signed-rank test (for fold change comparisons) was used, depending on data
565 type and normality. For comparisons among multiple groups, either one-way ANOVA with
566 Tukey's multiple comparisons test or the Kruskal-Wallis test with Dunn's correction was used,
567 as appropriate. Significant outliers were excluded using the ROUT test (Q=1%). A *p*-value of
568 <0.05 was considered statistically significant.

569 **DATA AVAILABILITY**

570 The datasets generated will be deposited in a publicly available repository upon acceptance
571 of the manuscript for publication.

572 **ACKNOWLEDGEMENTS**

573 We are grateful to the team members of the Biological Service Unit, Flow Cytometry Facility
574 and Breast Cancer Now Histopathology Core Facility at The Institute of Cancer Research for
575 technical assistance. This work was supported by the Wellcome Trust, Oracle Cancer Trust,
576 The Institute of Cancer Research/Royal Marsden Hospital (ICR/RM) Centre for
577 Immunotherapy of Cancer, ICR/RM NIHR Biomedical Research Centre (IS-BRC-1215-
578 20021), Cancer Research UK (CRUK) Head and Neck Programme Grant (DRCRPG-
579 Nov22/100008) and ICR/RM CRUK RadNet Centre of Excellence (C7224/A28724).

580 **MATERIALS & CORRESPONDENCE**

581 Correspondence and requests for materials should be addressed to Dr Charleen Chan Wah
582 Hak, Division of Radiotherapy and Imaging, The Institute of Cancer Research, Chester Beatty
583 Laboratories, 237 Fulham Road, London SW3 6JB (charleen.chan@icr.ac.uk).

584 **AUTHOR CONTRIBUTIONS**

585 C.CWH., A.A.M., K.J.H., and A.R. contributed to the conception and design of the research
586 as well as in writing the manuscript. C.CWH., A.R., E.C.P., V.R., L.C.H., M.G., E.S.A., S.F.,
587 I.D., A.B., J.N.K., H.B., C.M., M.P. performed the experiments and acquired data. A.P.
588 provided bioinformatic analysis. C.CWH., A.R., E.C.P., A.P. and M.O. contributed to the
589 analysis and interpretation of data. J.Y.L., P.N., H.N., M.C.U.C. and S.B. contributed to the

collection and provision of clinical samples. M.O. provided the supply of Nr4a3-Tocky mice and Tocky data analysis bioinformatic pipelines. A.A.M. and K.J.H. provided funding for the project. A.A.M., K.J.H., and M.O. are the guarantors and joint senior authors of this work. All authors read and approved the final manuscript.

COMPETING INTEREST

The authors declare no relevant competing interests.

REFERENCES

1. Mellman I, Chen DS, Powles T, Turley SJ. The cancer-immunity cycle: Indication, genotype, and immunotype. Immunity. 2023;56(10):2188-205.
2. Schietinger A, Philip M, Krisnawan VE, Chiu EY, Delrow JJ, Basom RS, et al. Tumor-Specific T Cell Dysfunction Is a Dynamic Antigen-Driven Differentiation Program Initiated Early during Tumorigenesis. Immunity. 2016;45(2):389-401.
3. Blank CU, Haining WN, Held W, Hogan PG, Kallies A, Lugli E, et al. Defining 'T cell exhaustion'. Nat Rev Immunol. 2019;19(11):665-74.
4. Im SJ, Hashimoto M, Gerner MY, Lee J, Kissick HT, Burger MC, et al. Defining CD8+ T cells that provide the proliferative burst after PD-1 therapy. Nature. 2016;537(7620):417-21.
5. Siddiqui I, Schaeuble K, Chennupati V, Fuertes Marraco SA, Calderon-Copete S, Pais Ferreira D, et al. Intratumoral Tcf1(+)PD-1(+)CD8(+) T Cells with Stem-like Properties Promote Tumor Control in Response to Vaccination and Checkpoint Blockade Immunotherapy. Immunity. 2019;50(1):195-211.e10.
6. Kallies A, Zehn D, Utzschneider DT. Precursor exhausted T cells: key to successful immunotherapy? Nat Rev Immunol. 2020;20(2):128-36.
7. Antonia SJ, Villegas A, Daniel D, Vicente D, Murakami S, Hui R, et al. Durvalumab after Chemoradiotherapy in Stage III Non-Small-Cell Lung Cancer. N Engl J Med. 2017;377(20):1919-29.
8. Zhou J, Wang G, Chen Y, Wang H, Hua Y, Cai Z. Immunogenic cell death in cancer therapy: Present and emerging inducers. J Cell Mol Med. 2019;23(8):4854-65.
9. Nenclares P, Larkeryd A, Manodoro F, Lee JY, Lalondrelle S, Gilbert DC, et al. T-cell receptor determinants of response to chemoradiation in locally-advanced HPV16-driven malignancies. Front Oncol. 2023;13:1296948.
10. Akiyoshi T, Gotoh O, Tanaka N, Kiyotani K, Yamamoto N, Ueno M, et al. T-cell complexity and density are associated with sensitivity to neoadjuvant chemoradiotherapy in patients with rectal cancer. Cancer Immunol Immunother. 2021;70(2):509-18.
11. Manzar GS, Alam MBE, Lynn EJ, Karpinets TV, Harris T, Lo D, et al. Exploratory analysis of the cervix tumoral HPV antigen-specific T-cell repertoire during chemoradiation and after brachytherapy. Brachytherapy. 2024;23(2):123-35.
12. Barsouk A, Aluru JS, Rawla P, Saginala K, Barsouk A. Epidemiology, Risk Factors, and Prevention of Head and Neck Squamous Cell Carcinoma. Med Sci (Basel). 2023;11(2).
13. Lacas B, Carmel A, Landais C, Wong SJ, Licitra L, Tobias JS, et al. Meta-analysis of chemotherapy in head and neck cancer (MACH-NC): An update on 107 randomized trials and 19,805 patients, on behalf of MACH-NC Group. Radiother Oncol. 2021;156:281-93.
14. Mehanna H, Robinson M, Hartley A, Kong A, Foran B, Fulton-Lieuw T, et al. Radiotherapy plus cisplatin or cetuximab in low-risk human papillomavirus-positive oropharyngeal cancer (De-ESCALaTE HPV): an open-label randomised controlled phase 3 trial. Lancet. 2019;393(10166):51-60.
15. Gillison ML, Trotti AM, Harris J, Eisbruch A, Harari PM, Adelstein DJ, et al. Radiotherapy plus cetuximab or cisplatin in human papillomavirus-positive oropharyngeal cancer (NRG Oncology RTOG 1016): a randomised, multicentre, non-inferiority trial. Lancet. 2019;393(10166):40-50.

16. Ferris RL, Flamand Y, Weinstein GS, Li S, Quon H, Mehra R, et al. Phase II Randomized Trial of Transoral Surgery and Low-Dose Intensity Modulated Radiation Therapy in Resectable p16+ Locally Advanced Oropharynx Cancer: An ECOG-ACRIN Cancer Research Group Trial (E3311). J Clin Oncol. 2022;40(2):138-49.
17. Gui C, Wray R, Schöder H, Deasy JO, Grkovski M, Humm JL, et al. Tumor Hypoxia on 18F-fluoromisonidazole Positron Emission Tomography and Distant Metastasis From Head and Neck Squamous Cell Carcinoma. JAMA Netw Open. 2024;7(9):e2436407.
18. Lee NYF, R. L. Psyrri, A., Haddad, R. I., Tahara M, Bourhis J, Harrington K, Chang PM, Lin JC, et al. Avelumab plus standard-of-care chemoradiotherapy versus chemoradiotherapy alone in patients with locally advanced squamous cell carcinoma of the head and neck: a randomised, double-blind, placebo-controlled, multicentre, phase 3 trial. Lancet Oncol. 2021;22(4):450-62.
19. Machiels J-P, Tao Y, Licitra L, Burtness B, Tahara M, Rischin D, et al. Pembrolizumab plus concurrent chemoradiotherapy versus placebo plus concurrent chemoradiotherapy in patients with locally advanced squamous cell carcinoma of the head and neck (KEYNOTE-412): a randomised, double-blind, phase 3 trial. The Lancet Oncology. 2024;25(5):572-87.
20. Tao Y, Aupérin A, Sun X, Sire C, Martin L, Coutte A, et al. Avelumab-cetuximab-radiotherapy versus standards of care in locally advanced squamous-cell carcinoma of the head and neck: The safety phase of a randomised phase III trial GORTEC 2017-01 (REACH). Eur J Cancer. 2020;141:21-9.
21. Haddad R, Fayette J, Teixeira M, Prabhash K, Mesia R, Kawecki A, et al. Atezolizumab in High-Risk Locally Advanced Squamous Cell Carcinoma of the Head and Neck: A Randomized Clinical Trial. Jama. 2025;333(18):1599-607.
22. Mehanna HM, Gaunt P, forster M, Kong A, Sen M, Hartley A, et al. 1317O Results from CompARE phase III RCT: Neoadjuvant durvalumab plus chemoradiotherapy (CRT) followed by adjuvant durvalumab immunotherapy (IO) vs CRT alone in intermediate and high-risk oropharyngeal cancer (OPC). Annals of Oncology. 2025;36:S824.
23. Cheng D, Qiu K, Rao Y, Mao M, Li L, Wang Y, et al. Proliferative exhausted CD8(+) T cells exacerbate long-lasting anti-tumor effects in human papillomavirus-positive head and neck squamous cell carcinoma. Elife. 2023;12.
24. Wang D, Fang J, Wen S, Li Q, Wang J, Yang L, et al. A comprehensive profile of TCF1(+) progenitor and TCF1(-) terminally exhausted PD-1(+)CD8(+) T cells in head and neck squamous cell carcinoma: implications for prognosis and immunotherapy. Int J Oral Sci. 2022;14(1):8.
25. Sievers C, Craveiro M, Friedman J, Robbins Y, Yang X, Bai K, et al. Phenotypic plasticity and reduced tissue retention of exhausted tumor-infiltrating T cells following neoadjuvant immunotherapy in head and neck cancer. Cancer Cell. 2023;41(5):887-902.e5.
26. Bending D, Ono M. From stability to dynamics: understanding molecular mechanisms of regulatory T cells through Foxp3 transcriptional dynamics. Clinical and experimental immunology. 2019;197(1):14-23.
27. Bending D, Paduraru A, Ducker CB, Prieto Martin P, Crompton T, Ono M. A temporally dynamic Foxp3 autoregulatory transcriptional circuit controls the effector Treg programme. The EMBO journal. 2018;37(16).
28. Bending D, Prieto Martin P, Paduraru A, Ducker C, Marzaganov E, Laviron M, et al. A timer for analyzing temporally dynamic changes in transcription during differentiation in vivo. The Journal of cell biology. 2018;217(8):2931-50.

29. Dolina JS, Van Braeckel-Budimir N, Thomas GD, Salek-Ardakani S. CD8(+) T Cell Exhaustion in Cancer. Front Immunol. 2021;12:715234.
30. Hashimoto M, Kamphorst AO, Im SJ, Kissick HT, Pillai RN, Ramalingam SS, et al. CD8 T Cell Exhaustion in Chronic Infection and Cancer: Opportunities for Interventions. Annu Rev Med. 2018;69:301-18.
31. Greiff V, Miho E, Menzel U, Reddy ST. Bioinformatic and Statistical Analysis of Adaptive Immune Repertoires. Trends Immunol. 2015;36(11):738-49.
32. Wu T, Ji Y, Moseman EA, Xu HC, Manglani M, Kirby M, et al. The TCF1-Bcl6 axis counteracts type I interferon to repress exhaustion and maintain T cell stemness. Sci Immunol. 2016;1(6).
33. Silva SL, Albuquerque AS, Serra-Caetano A, Foxall RB, Pires AR, Matoso P, et al. Human naïve regulatory T-cells feature high steady-state turnover and are maintained by IL-7. Oncotarget. 2016;7(11):12163-75.
34. Shevyrev D, Tereshchenko V. Treg Heterogeneity, Function, and Homeostasis. Front Immunol. 2019;10:3100.
35. Satoh M, Seki S, Hashimoto W, Ogasawara K, Kobayashi T, Kumagai K, et al. Cytotoxic gammadelta or alphabeta T cells with a natural killer cell marker, CD56, induced from human peripheral blood lymphocytes by a combination of IL-12 and IL-2. J Immunol. 1996;157(9):3886-92.
36. Barnaba V, Franco A, Paroli M, Benvenuto R, De Petrillo G, Burgio VL, et al. Selective expansion of cytotoxic T lymphocytes with a CD4+CD56+ surface phenotype and a T helper type 1 profile of cytokine secretion in the liver of patients chronically infected with Hepatitis B virus. J Immunol. 1994;152(6):3074-87.
37. Holmen Olofsson G, Pedersen SR, Aehnlich P, Svane IM, Idorn M, Thor Straten P. The capacity of CD4(+) Vγ9Vδ2 T cells to kill cancer cells correlates with co-expression of CD56. Cytotherapy. 2021;23(7):582-9.
38. Scott AC, Dündar F, Zumbo P, Chandran SS, Klebanoff CA, Shakiba M, et al. TOX is a critical regulator of tumour-specific T cell differentiation. Nature. 2019;571(7764):270-4.
39. Khan O, Giles JR, McDonald S, Manne S, Ngiow SF, Patel KP, et al. TOX transcriptionally and epigenetically programs CD8(+) T cell exhaustion. Nature. 2019;571(7764):211-8.
40. Beltra JC, Manne S, Abdel-Hakeem MS, Kurachi M, Giles JR, Chen Z, et al. Developmental Relationships of Four Exhausted CD8(+) T Cell Subsets Reveals Underlying Transcriptional and Epigenetic Landscape Control Mechanisms. Immunity. 2020;52(5):825-41.e8.
41. Utzschneider DT, Gabriel SS, Chisanga D, Gloury R, Gubser PM, Vasanthakumar A, et al. Early precursor T cells establish and propagate T cell exhaustion in chronic infection. Nat Immunol. 2020;21(10):1256-66.
42. Ji D, Song C, Li Y, Xia J, Wu Y, Jia J, et al. Combination of radiotherapy and suppression of Tregs enhances abscopal antitumor effect and inhibits metastasis in rectal cancer. J Immunother Cancer. 2020;8(2).
43. Charpentier M, Formenti S, Demaria S. CD40 agonism improves anti-tumor T cell priming induced by the combination of radiation therapy plus CTLA4 inhibition and enhances tumor response. Oncoimmunology. 2023;12(1):2258011.
44. Dillon MT, Patin EC, Mohammed K, Guevara J, Smith SA, Dean E, et al. Tumor control and immune activation through palliative irradiation and ATR inhibition, PATRIOT Part C: a phase Ib trial. Nat Commun. 2025;16(1):7064.

45. Judd NP, Winkler AE, Murillo-Sauca O, Brotman JJ, Law JH, Lewis JS, et al. ERK1/2 regulation of CD44 modulates oral cancer aggressiveness. Cancer Res. 2012;72(1):365-74.
46. Patro R, Duggal G, Love MI, Irizarry RA, Kingsford C. Salmon provides fast and bias-aware quantification of transcript expression. Nat Methods. 2017;14(4):417-9.
47. Soneson C, Love MI, Robinson MD. Differential analyses for RNA-seq: transcript-level estimates improve gene-level inferences. F1000Res. 2015;4:1521.
48. Love MI, Huber W, Anders S. Moderated estimation of fold change and dispersion for RNA-seq data with DESeq2. Genome Biol. 2014;15(12):550.
49. Puram SV, Mints M, Pal A, Qi Z, Reeb A, Gelev K, et al. Cellular states are coupled to genomic and viral heterogeneity in HPV-related oropharyngeal carcinoma. Nat Genet. 2023;55(4):640-50.
50. Hänzelmann S, Castelo R, Guinney J. GSVA: gene set variation analysis for microarray and RNA-seq data. BMC Bioinformatics. 2013;14:7.
51. Xu S, Hu E, Cai Y, Xie Z, Luo X, Zhan L, et al. Using clusterProfiler to characterize multiomics data. Nat Protoc. 2024;19(11):3292-320.

761 **FIGURE LEGENDS**

762 **Fig. 1: Both radiotherapy (RT) and chemoradiotherapy (CRT) increase CD8$^+$ T-cell**
763 **infiltration into tumours, but therapy is only CD8$^+$ T-cell dependent in CRT.**
764 Experiments performed in the mEER model. **A.** Tumour growth curves across indicated
765 treatment conditions. **B.** Survival curves across indicated treatment conditions (A-B: Vehicle
766 n=11, Cisplatin n=11, RT + vehicle n=11, CRT n=12; 2 independent experiments). **C.** Absolute
767 change of CD8$^+$ T-cell counts/mg tumour vs average of timematched controls across indicated
768 timepoints post-RT as measured by flow cytometry (RT d3 n = 9, RT d7 n = 15, RT d10 n =
769 17, RT d14 n = 6; 6 independent experiments of 2 consecutive timepoints). **D.** CD8$^+$ T-cells/
770 mm^2 tumour at 14 days post-RT by immunohistochemistry, necrotic regions excluded,
771 quantified by QuPath v. 0.3.0. (Vehicle n=13, RT, n=16, CRT n=11; 3 independent
772 experiments). **E.** CD8$^+$ T-cell count/ mg of tumour by flow cytometry (Vehicle n=10, Cisplatin
773 n=11, RT n=10, CRT n=11; 2 independent experiments). **F.** Percentage of PD-1^{hi} CD8$^+$ T-cells
774 by flow cytometry (Vehicle n=11, Cisplatin n=12, RT n=11, CRT n=12; 2 independent
775 experiments). **G-H:** Tumour growth curves of αCD8 depletion experiments, with mice receiving
776 either RT **(G)** or CRT **(H)** (Vehicle + isotype n=6, RT + isotype n=6, RT + αCD8 n = 5, CRT +
777 isotype n = 6, CRT + αCD8 n = 6; data from 1 experiment). Results are means ± SEM and *n*
778 denotes mice per group. Parametric statistics were only applied to normally distributed data
779 (Shapiro-Wilk test). P-values shown were determined by the log-rank (Mantel–Cox) (B),
780 Kruskal Wallis test with Dunn's multiple comparisons test (C-E), Ordinary one-way ANOVA
781 with Tukey's multiple comparisons test (F) and Two-tailed Unpaired t test (H).
782

783 **Fig. 2: T-cell dynamics reveals differences in tumour T-cell populations between RT and**
784 **CRT, with a reduced percentage increase in persistently engaged CD8$^+$ T-cells in CRT**
785 **versus RT.**
786 **A.** Schematic of the treatment timeline in Nr4a3-Tocky mEER tumour-bearing mice. *Created*
787 *with Biorender.com.* **B-F:** UMAP analysis of CD8$^+$ tumour-infiltrating lymphocytes (TILs),
788 results concatenated from 30 mice (Vehicle n=7, Cisplatin n=8, RT + vehicle n=7, CRT n=8;
789 1 experiment). **(B)** UMAP plot showing distribution of clusters 1–8 across treatment conditions.
790 **(C)** Selected clusters 2, 3, 4 and 5 showing significant differences between treatment groups
791 (Vehicle n=7, Cisplatin n=8, RT + vehicle n=7, CRT n=8). **(D)** Timer fluorescence patterns
792 within clusters 2, 3, 4 and 5. Cluster 3 is defined by a persistent-arrested (PAt) Tocky profile
793 with high activation and immune checkpoint expression. **(E)** Heatmap overlays of Tocky
794 "angle" (antigen engagement), "intensity" (TCR signalling strength). **(F)** Histograms illustrating
795 marker expression by cluster. **G.** Percentage change in PAt CD8$^+$ T-cells (% ΔPAt) in RT +
796 vehicle and CRT groups versus the average of vehicle group (RT + vehicle n=11, CRT n=12;

797 2 independent experiments). Results are means ± SEM and *n* denotes mice per group.
798 Parametric statistics were only applied to normally distributed data (Shapiro-Wilk test). P-
799 values shown were determined by Ordinary one-way ANOVA with Tukey's multiple
800 comparisons test (E: cluster 2-3), Kruskal Wallis test with Dunn's multiple comparisons test
801 (E: cluster 4-5) and Two-tailed Unpaired t test (G). Significant outliers were removed via ROUT
802 test (Q = 1%). All data are representative of two independent experiments.
803
804 **Fig. 3: CRT increases antigen-engaged TILs with effector memory over naïve phenotype**
805 **compared to RT; persistently engaged T-cells show higher inhibitory checkpoint**
806 **expression linked to exhaustion.**
807 **A.** Experimental schema: Single-cell analysis was performed on tumour-infiltrating
808 lymphocytes (TILs) from tumours (Tum) or TDLN harvested from mEER-bearing Nr4a3-Tocky
809 mice treated with vehicle (Veh), RT or CRT. Cells were sorted according to Tocky antigen-
810 engagement profile prior to integrated single-cell analyses (Vehicle n=12, RT n=12, CRT
811 n=12; 1 experiment). **B-H:** Cells were subject to UMAP clustering based on Abseq expression
812 profile. **(B)** UMAP by sample tag. **(C)** Cell annotation of T-cell subtype: CD4, CD8, DN (double
813 negative) and DP (double positive). **(D)** Functional T-cell subtype annotation based on
814 expression markers: T_N (naïve, $CD62L^+$), T_{CM} (central memory, $CD62L^+$, $CD44^+$), T_{EM} (effector
815 memory, $CD62L^-$ $CD44^+$). **(E)** Heatmap of selected Abseq marker expression overlaid on
816 UMAP. **(F)** Dot plot of Abseq marker expression in TILs by treatment. **(G)** Distribution of Tocky
817 populations: "persistent" (pers), "arrested" (arr) and "timer negative" (neg) within the UMAP
818 space. **(H)** Dot plots of Abseq marker expression across different Tocky populations in TILs.
819
820 **Fig. 4: CRT leads to more focused, expanded CD8+ T-cell populations with an effector**
821 **profile than RT.**
822 Single-cell TCR sequencing was performed on sorted tumour-infiltrating lymphocytes (TILs)
823 from tumours (Tum) or TDLN harvested from mEER-bearing mice treated with vehicle (Veh),
824 RT or CRT (Vehicle n=12, RT n=12, CRT n=12, 1 experiment). **A.** Distribution of T-cell clonal
825 expansion within UMAP space, categorised by clone frequency within the total TCR repertoire:
826 hyperexpanded (>20 and ≤100), large (>5 and ≤20), medium (>2 and ≤5), small (>1 and ≤2)
827 and single (>0 and ≤1). Cells without information on paired TCR α (alpha) and β (beta) chain
828 CDR3 (Complementarity-Determining Region 3) sequence information are denoted by "NA".
829 **B.** Three CDR3 sequences which were hyperexpanded. **C.** Distribution of categories of clonal
830 expansion within UMAP space by sample type and treatment group. **D.** Categories of clonal
831 expansion by sample type and treatment group by proportion of cells **E.** Clonal diversity
832 dotplots comparing various diversity indices between Tum_RT and Tum_CRT: Shannon;

833 Inverse (Inv) Simpson; Chao1 (Chao) Abundance-based Coverage Estimator (ACE) and Inv
834 Pielou. **F.** Proportions of T-cell type (CD4+, CD8+, double negative [DN], double positive [DP])
835 by categories of clonal expansion. **G.** Abseq expression marker profile across different clonal
836 expansion categories.
837
838 **Fig. 5: CRT leads to greater clonal expansion of antigen-engaged T-cells than RT, and**
839 **clonal CD8 TILs treated with CRT show relative acquisition of a less exhausted**
840 **phenotype on transition from persistent ("pers"), to historical, T-cell engagement**
841 **("arr").**
842 Single-cell analysis was performed on sorted tumour-infiltrating lymphocytes (TILs) from
843 tumours (Tum) or TDLN harvested from mEER-bearing mice treated with vehicle (Veh), RT or
844 CRT (Vehicle n=12, RT n=12, CRT n=12, 1 experiment). **A.** Distribution of Tocky populations
845 within UMAP space according to categories of clonal expansion: "new", "persistent" (pers),
846 "arrested" (arr) and "timer negative" (neg). **B.** Proportions of cells undergoing clonal expansion
847 by Tocky population. **C-E:** Abseq marker expression profile of various TILs subsets: **(C)** Clonal
848 (≥ 5) and "persistent" $CD8^+$ TILs by treatment type, **(D)** Clonal (≥ 5) $CD8^+$ TILs from mice
849 treated with CRT (Tum_CRT) by Tocky population and **(E)** Clonal (≥ 5) $CD4^+$ TILs treated with
850 CRT (Tum_CRT) by Tocky population.
851
852 **Fig. 6: CRT increases the proportion and clonal expansion of precursor exhausted**
853 **(T_{PEX}) to terminally exhausted (T_{EX}) CD8+ TILs in the arrested phase, compared to RT**
854 **alone.**
855 Single-cell analysis whereby cells were subject to UMAP clustering based on transcriptomic
856 profile (Vehicle n=12, RT n=12, CRT n=12, 1 experiment; only available for Tocky arrested
857 ["arr"] and timer negative ["neg"] samples). **A.** Dot plot illustrating relative gene expression
858 across different T-cell subgroups (each corresponding to a UMAP cluster) and gene
859 categories. Dot colour intensity represents the average expression level, while dot size
860 indicates the percentage of cells expressing the gene. **B.** Cell annotation of clusters by T-cell
861 subgroups. **C-D.** Cell type composition by treatment group and Tocky stage "arr" or "neg" of
862 tumour samples **(C)** and tumour-draining lymph nodes (TDLN) **(D)**. **E.** Clone size categories
863 indicated by clone frequency within the total TCR repertoire: hyperexpanded (>20 and ≤100),
864 large (>5 and ≤20), medium (>2 and ≤5), small (>1 and ≤2) and single (>0 and ≤1). Cells
865 without CDR3 sequence information are denoted by "CDR3 NA". **F-G:** Barplots illustrating
866 percentage of cells within each clone size category by cell type cluster for "arr" Tum_CRT **(F)**
867 and Tum_RT **(G)**. Abbreviations: Tpex; precursor exhausted T-cells, cyto, cytotoxic; Tex,
868 terminally exhausted T-cells; Treg, regulatory T-cells; T DN, double negative T-cells; Inhib.

869 Receptors, inhibitory receptors; Co-stim. activation; co-stimulatory/ activation; eff. molecules;
870 effector molecules; TFs, transcription factors.
871
872 **Fig 7: CRT versus RT differentially modulates T-cell subsets and exhaustion**
873 **trajectories in human PBMCs.**
874 Peripheral blood mononuclear cells (PBMCs) were collected from patients with LA-SCCHN
875 receiving definitive RT (n=4) or CRT (n=8) as part of the INOVATE study (ISRCTN32335415)
876 at baseline (BL), week 3 of RT (RTW3), and 3 months post-treatment (RTFU; one RT patient
877 at 6 weeks). Flow cytometry analysis of PBMCs was performed. **A.** Frequencies of T-cell
878 subsets over time, comparing RT and CRT. **B-F.** Fold changes relative to baseline at RTW3
879 and RTFU shown as min-to-max box-and-whisker plots with all points displayed, for $CD8^+$ T-
880 cells **(B)**, Granzyme B^+ ($GrzmB^+$) $CD8^+$ T-cells and $CD56^+$ Tconv **(C)**, $Ki67^+$ Tregs **(D)**, PD-1^+
881 expression on $CD8^+$ and Tconv **(E)**, terminally exhausted (T_{EX}; TOX^+ TCF-1^- PD-1^{hi}) and
882 progenitor exhausted (T_{PEX}; TCF-1^+ TOX^- PD-1^{int}) $CD8^+$ T-cell populations **(F)**. Statistical
883 significance for fold change comparisons in panels B-F was assessed using the Wilcoxon
884 signed-rank test; $p<0.05$.

Figure 1

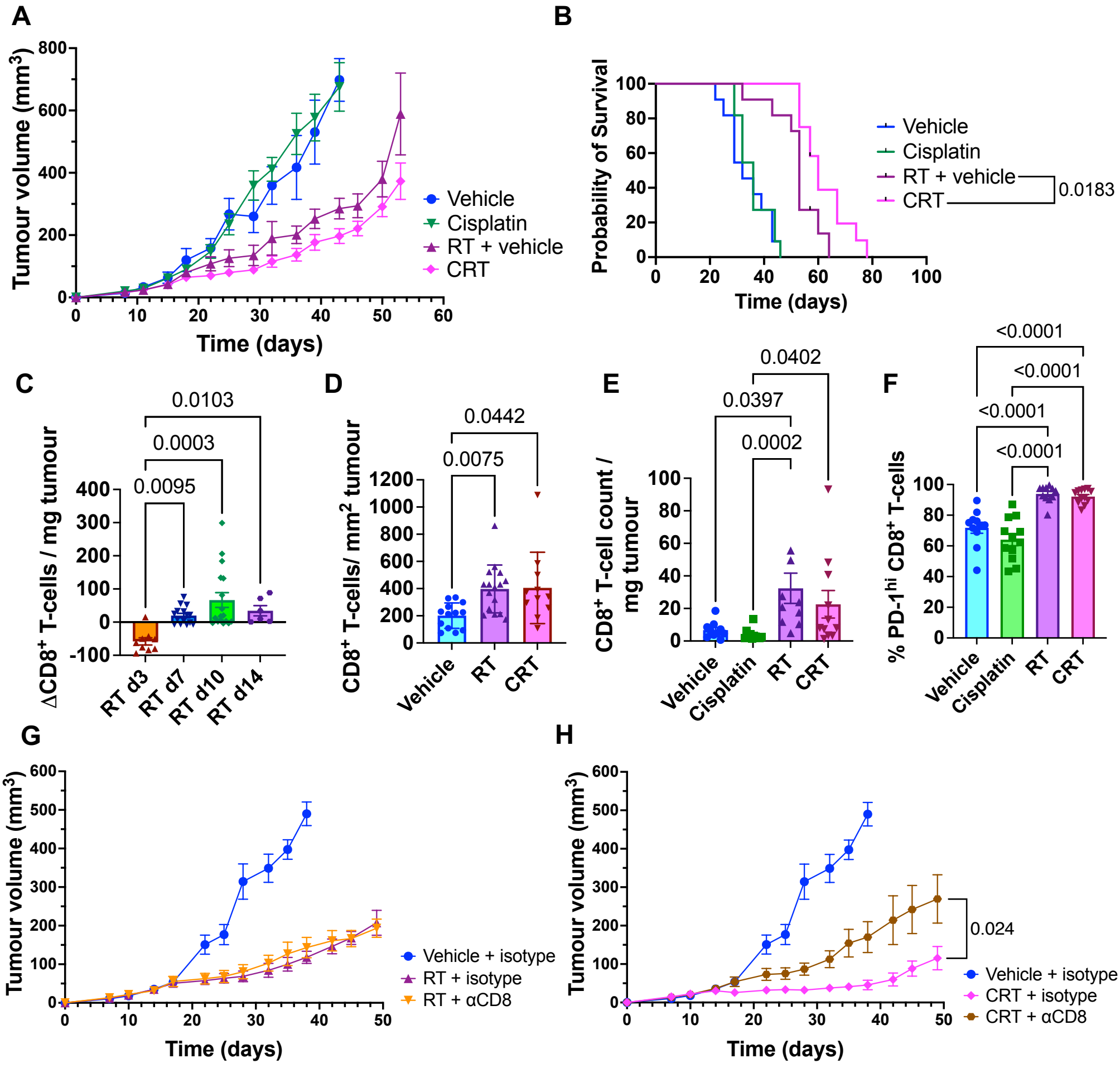
A
Tumour volume (mm3)
Time (days)
Vehicle
Cisplatin
RT + vehicle
CRT
B
Probability of Survival
Time (days)
Vehicle
Cisplatin
RT + vehicle
CRT
0.0183
C
ΔCD8+ T-cells / mg tumour
0.0103
0.0003
0.0095
RT d3
RT d7
RT d10
RT d14
D
CD8+ T-cells/ mm2 tumour
0.0442
0.0075
Vehicle
RT
CRT
E
CD8+ T-cell count / mg tumour
0.0402
0.0397
0.0002
Vehicle
Cisplatin
RT
CRT
F
% PD-1hi CD8+ T-cells
<0.0001
<0.0001
<0.0001
<0.0001
Vehicle
Cisplatin
RT
CRT
G
Tumour volume (mm3)
Time (days)
Vehicle + isotype
RT + isotype
RT + αCD8
H
Tumour volume (mm3)
Time (days)
0.024
Vehicle + isotype
CRT + isotype
CRT + αCD8

Figure 2

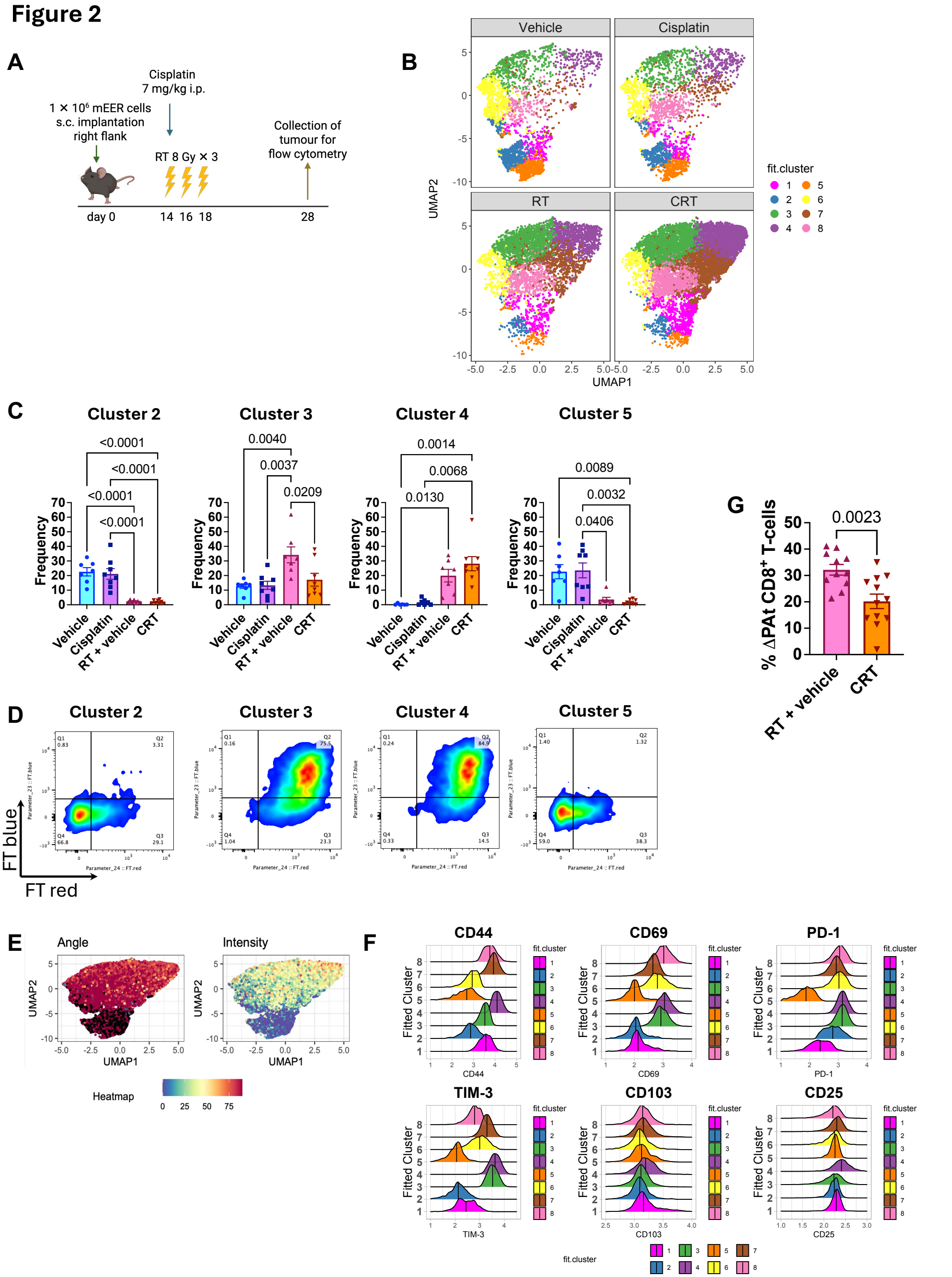
A
Cisplatin
7 mg/kg i.p.
1 × 10⁶ mEER cells
s.c. implantation
right flank
RT 8 Gy × 3
Collection of
tumour for
flow cytometry
day 0
14 16 18
28
B
Vehicle
Cisplatin
RT
CRT
UMAP2
UMAP1
fit.cluster
C
Cluster 2
Cluster 3
Cluster 4
Cluster 5
Frequency
Vehicle
Cisplatin
RT + vehicle
CRT
G
% ΔPAt CD8⁺ T-cells
0.0023
D
FT blue
FT red
E
Angle
Intensity
Heatmap
F
CD44
CD69
PD-1
TIM-3
CD103
CD25
Fitted Cluster

Figure 3

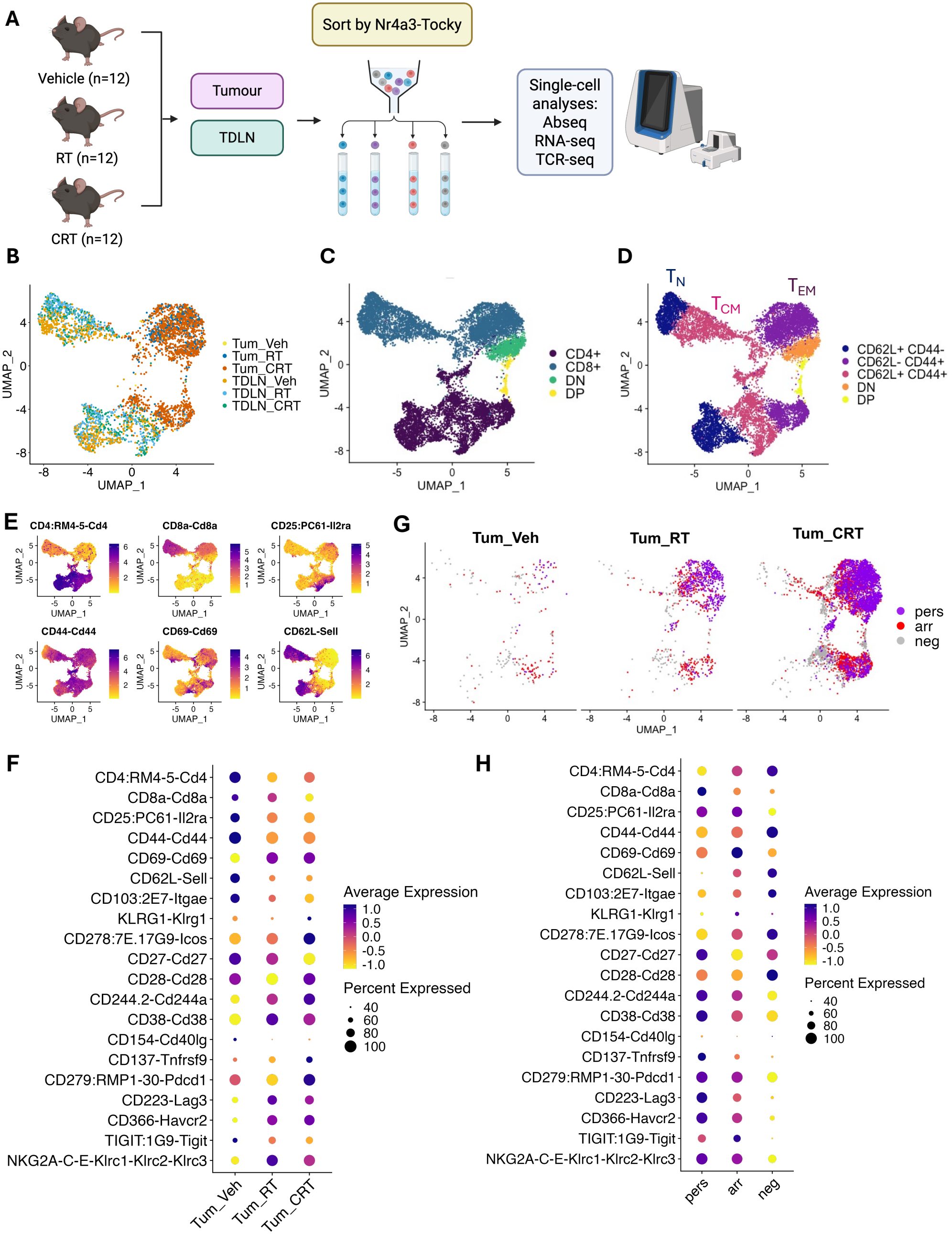
A
Vehicle (n=12)
RT (n=12)
CRT (n=12)
Tumour
TDLN
Sort by Nr4a3-Tocky
Single-cell analyses: Abseq RNA-seq TCR-seq
B
UMAP_2
UMAP_1
Tum_Veh
Tum_RT
Tum_CRT
TDLN_Veh
TDLN_RT
TDLN_CRT
C
CD4+
CD8+
DN
DP
D
T_N
T_{CM}
T_{EM}
CD62L+ CD44-
CD62L- CD44+
CD62L+ CD44+
DN
DP
E
CD4:RM4-5-Cd4
CD8a-Cd8a
CD25:PC61-Il2ra
CD44-Cd44
CD69-Cd69
CD62L-Sell
G
Tum_Veh
Tum_RT
Tum_CRT
pers
arr
neg
F
CD4:RM4-5-Cd4
CD8a-Cd8a
CD25:PC61-Il2ra
CD44-Cd44
CD69-Cd69
CD62L-Sell
CD103:2E7-Itgae
KLRG1-Klrg1
CD278:7E.17G9-Icos
CD27-Cd27
CD28-Cd28
CD244.2-Cd244a
CD38-Cd38
CD154-Cd40lg
CD137-Tnfrsf9
CD279:RMP1-30-Pdcd1
CD223-Lag3
CD366-Havcr2
TIGIT:1G9-Tigit
NKG2A-C-E-Klrc1-Klrc2-Klrc3
Tum_Veh
Tum_RT
Tum_CRT
Average Expression
Percent Expressed
H
pers
arr
neg

Figure 4

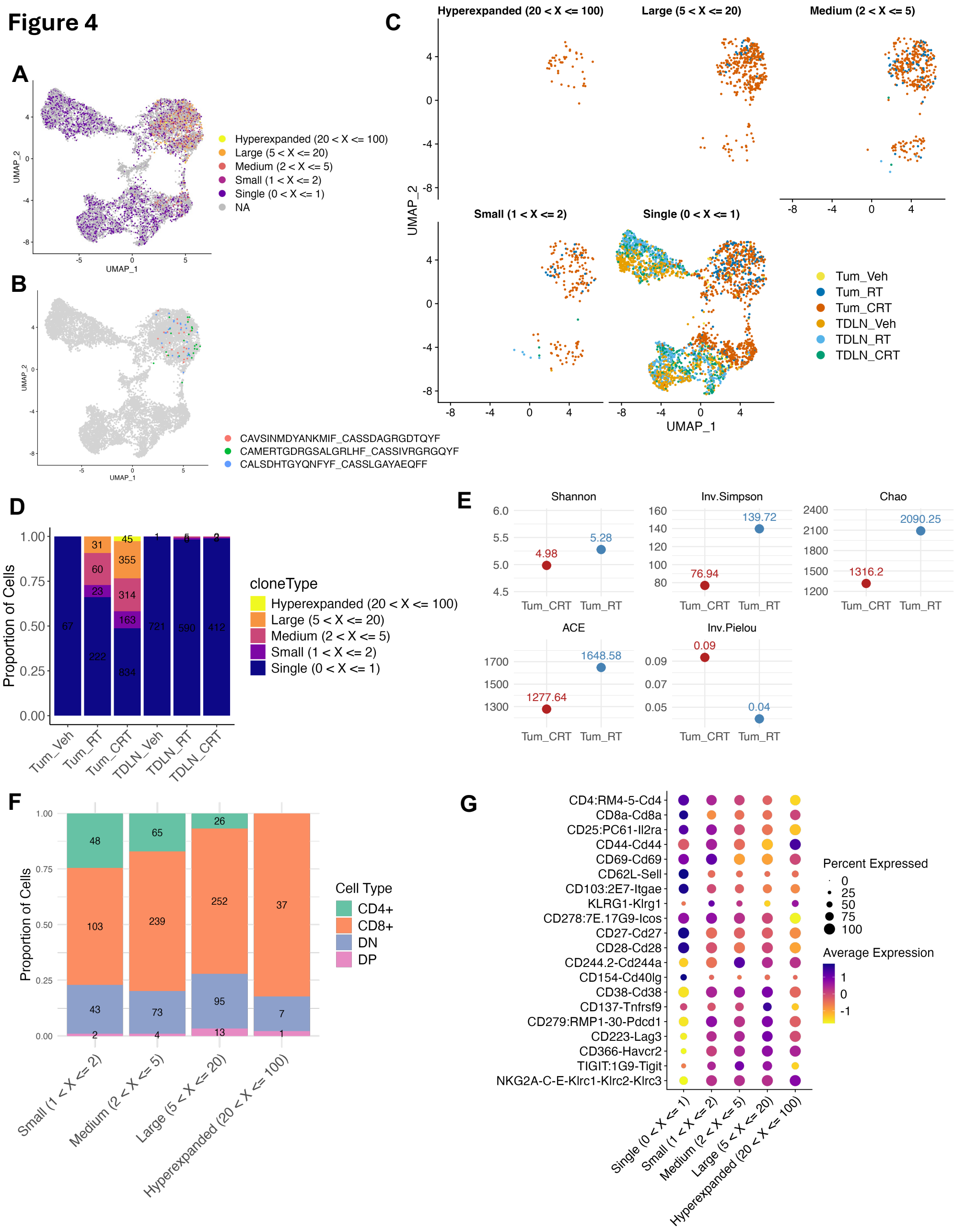
A
UMAP_2
UMAP_1
Hyperexpanded (20 < X <= 100)
Large (5 < X <= 20)
Medium (2 < X <= 5)
Small (1 < X <= 2)
Single (0 < X <= 1)
NA
B
CAVSINMDYANKMIF_CASSDAGRGDTQYF
CAMERTGDRGSALGRLHF_CASSIVRGRGQYF
CALSDHTGYQNFYF_CASSLGAYAEQFF
C
Hyperexpanded (20 < X <= 100)
Large (5 < X <= 20)
Medium (2 < X <= 5)
Small (1 < X <= 2)
Single (0 < X <= 1)
Tum_Veh
Tum_RT
Tum_CRT
TDLN_Veh
TDLN_RT
TDLN_CRT
D
Proportion of Cells
cloneType
Hyperexpanded (20 < X <= 100)
Large (5 < X <= 20)
Medium (2 < X <= 5)
Small (1 < X <= 2)
Single (0 < X <= 1)
E
Shannon
Inv.Simpson
Chao
ACE
Inv.Pielou
4.98
5.28
76.94
139.72
1316.2
2090.25
1277.64
1648.58
0.09
0.04
Tum_CRT
Tum_RT
F
Proportion of Cells
Cell Type
CD4+
CD8+
DN
DP
Small (1 < X <= 2)
Medium (2 < X <= 5)
Large (5 < X <= 20)
Hyperexpanded (20 < X <= 100)
G
CD4:RM4-5-Cd4
CD8a-Cd8a
CD25:PC61-Il2ra
CD44-Cd44
CD69-Cd69
CD62L-Sell
CD103:2E7-Itgae
KLRG1-Klrg1
CD278:7E.17G9-Icos
CD27-Cd27
CD28-Cd28
CD244.2-Cd244a
CD154-Cd40lg
CD38-Cd38
CD137-Tnfrsf9
CD279:RMP1-30-Pdcd1
CD223-Lag3
CD366-Havcr2
TIGIT:1G9-Tigit
NKG2A-C-E-Klrc1-Klrc2-Klrc3
Single (0 < X <= 1)
Small (1 < X <= 2)
Medium (2 < X <= 5)
Large (5 < X <= 20)
Hyperexpanded (20 < X <= 100)
Percent Expressed
Average Expression

Figure 5

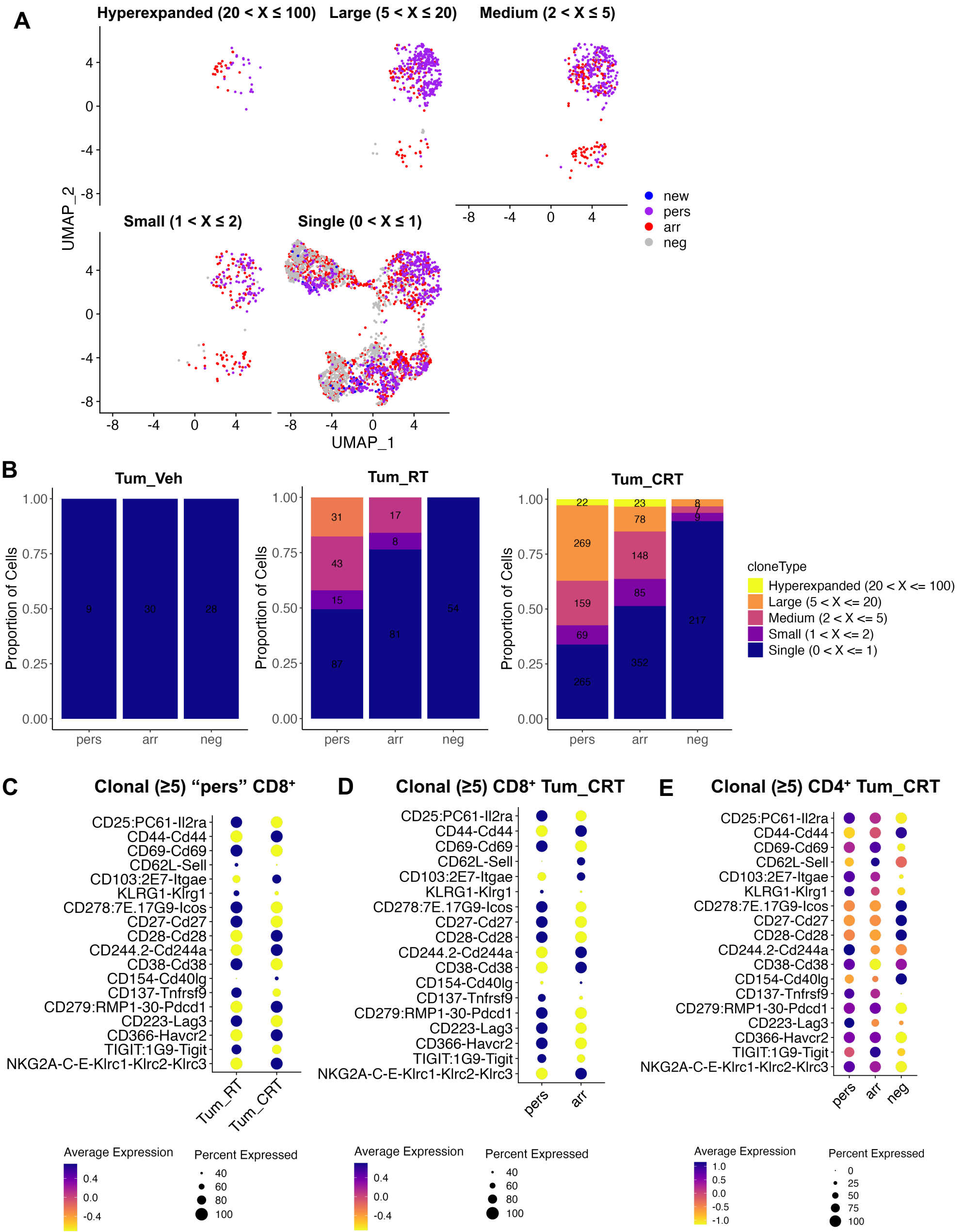
A
Hyperexpanded (20 < X ≤ 100)
Large (5 < X ≤ 20)
Medium (2 < X ≤ 5)
Small (1 < X ≤ 2)
Single (0 < X ≤ 1)
UMAP_2
UMAP_1
new
pers
arr
neg
B
Tum_Veh
Tum_RT
Tum_CRT
Proportion of Cells
pers
arr
neg
cloneType
Hyperexpanded (20 < X <= 100)
Large (5 < X <= 20)
Medium (2 < X <= 5)
Small (1 < X <= 2)
Single (0 < X <= 1)
C
Clonal (≥5) "pers" CD8+
D
Clonal (≥5) CD8+ Tum_CRT
E
Clonal (≥5) CD4+ Tum_CRT
CD25:PC61-Il2ra
CD44-Cd44
CD69-Cd69
CD62L-Sell
CD103:2E7-Itgae
KLRG1-Klrg1
CD278:7E.17G9-Icos
CD27-Cd27
CD28-Cd28
CD244.2-Cd244a
CD38-Cd38
CD154-Cd40lg
CD137-Tnfrsf9
CD279:RMP1-30-Pdcd1
CD223-Lag3
CD366-Havcr2
TIGIT:1G9-Tigit
NKG2A-C-E-Klrc1-Klrc2-Klrc3
Tum_RT
Tum_CRT
Average Expression
Percent Expressed

Figure 6

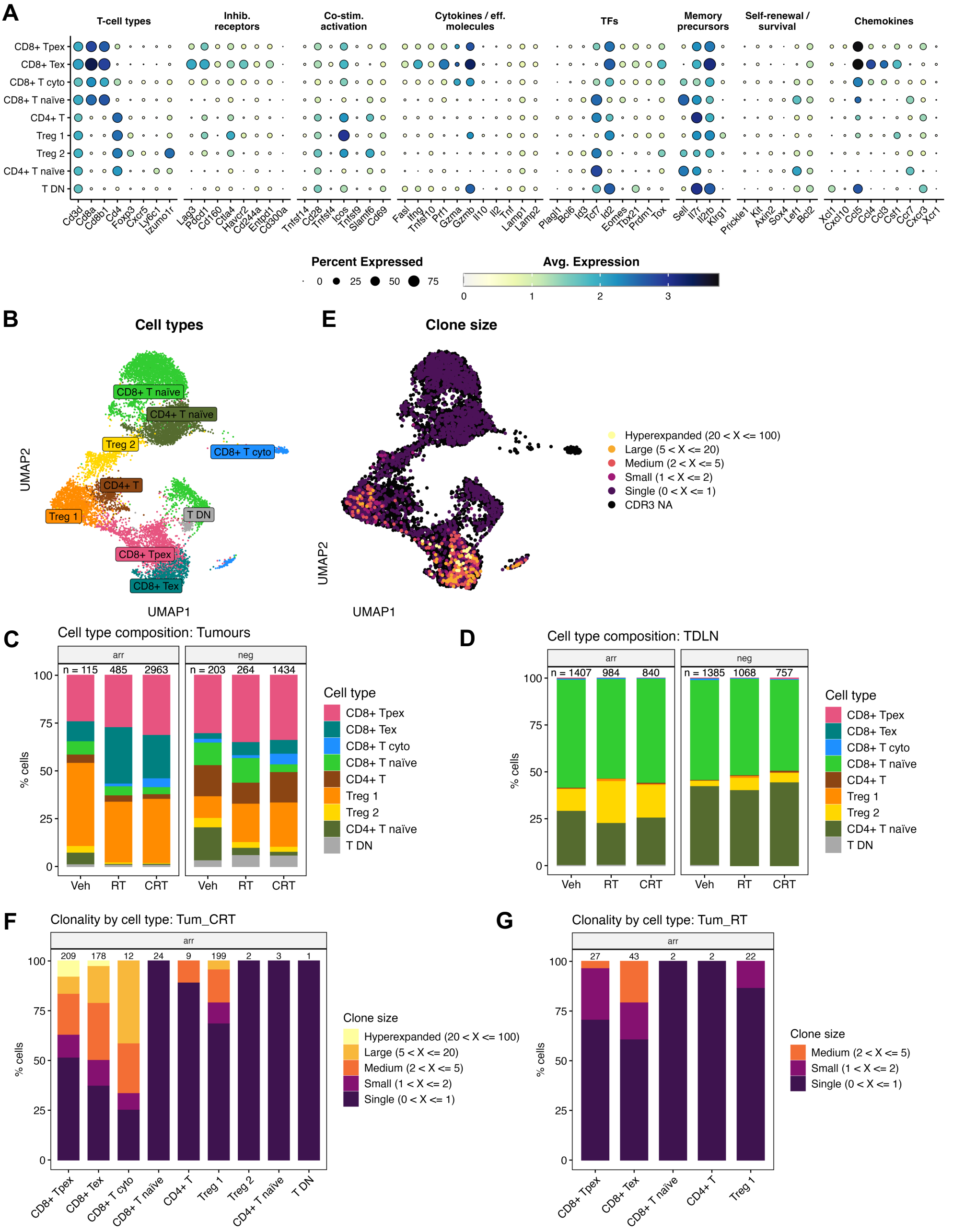
A
T-cell types
Inhib. receptors
Co-stim. activation
Cytokines / eff. molecules
TFs
Memory precursors
Self-renewal / survival
Chemokines
CD8+ Tpex
CD8+ Tex
CD8+ T cyto
CD8+ T naïve
CD4+ T
Treg 1
Treg 2
CD4+ T naïve
T DN
Cd3d Cd8a Cd8b1 Cd4 Foxp3 Cxcr5 Ly6c1 Izumo1r
Lag3 Pdcd1 Cd160 Cd1a4 Havcr2 Cd244a Entpd1 Cd300a
Tnfsf14 Cd28 Tnfsf4 Icos Tnfsf9 Slamf6 Cd69
Fasl Ifng Tnfsf10 Prf1 Gzma Gzmb Il10 Il2 Tnf Lamp1 Lamp2
Plagl1 Bcl6 Id3 Tcf7 Id2 Eomes Tbx21 Prdm1 Tox
Sell Il7r Il2rb Klrg1
Prickle1 Kit Axin2 Sox4 Lef1 Bcl2
Xcl1 Cxcl10 Ccl5 Ccl4 Ccl3 Csf1 Ccr7 Cxcr3 Xcr1
Percent Expressed
0 25 50 75
Avg. Expression
0 1 2 3
B
Cell types
CD8+ T naïve
CD4+ T naïve
Treg 2
CD8+ T cyto
CD4+ T
Treg 1
T DN
CD8+ Tpex
CD8+ Tex
UMAP2
UMAP1
E
Clone size
Hyperexpanded (20 < X <= 100)
Large (5 < X <= 20)
Medium (2 < X <= 5)
Small (1 < X <= 2)
Single (0 < X <= 1)
CDR3 NA
UMAP2
UMAP1
C
Cell type composition: Tumours
arr
neg
n = 115 485 2963
n = 203 264 1434
% cells
Veh RT CRT
Cell type
CD8+ Tpex
CD8+ Tex
CD8+ T cyto
CD8+ T naïve
CD4+ T
Treg 1
Treg 2
CD4+ T naïve
T DN
D
Cell type composition: TDLN
n = 1407 984 840
n = 1385 1068 757
F
Clonality by cell type: Tum_CRT
209 178 12 24 9 199 2 3 1
Clone size
Hyperexpanded (20 < X <= 100)
Large (5 < X <= 20)
Medium (2 < X <= 5)
Small (1 < X <= 2)
Single (0 < X <= 1)
CD8+ Tpex CD8+ Tex CD8+ T cyto CD8+ T naïve CD4+ T Treg 1 Treg 2 CD4+ T naïve T DN
G
Clonality by cell type: Tum_RT
27 43 2 2 22
CD8+ Tpex CD8+ Tex CD8+ T naïve CD4+ T Treg 1

Figure 7

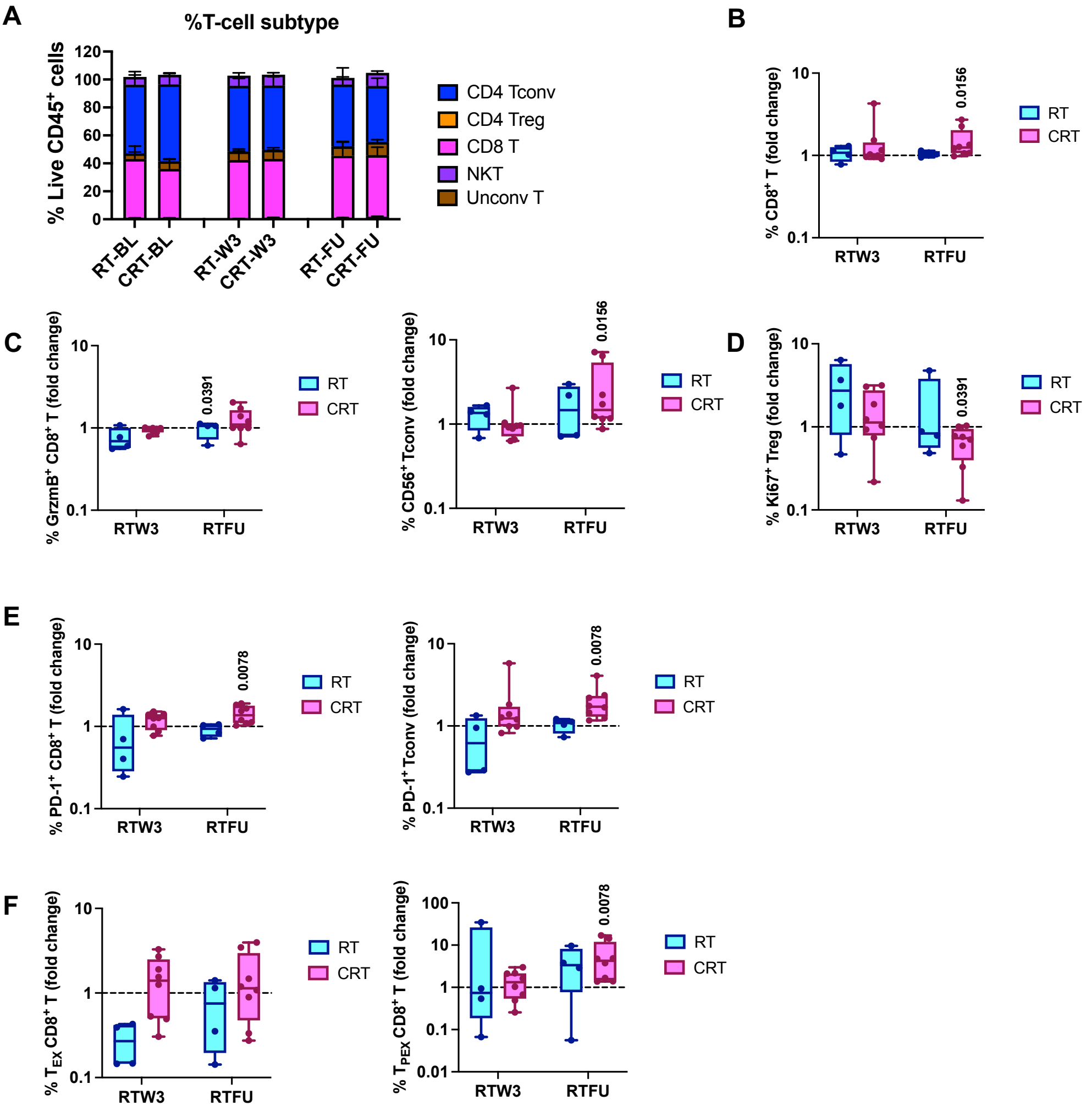
A
%T-cell subtype
% Live CD45+ cells
120
100
80
60
40
20
0
RT-BL
CRT-BL
RT-W3
CRT-W3
RT-FU
CRT-FU
CD4 Tconv
CD4 Treg
CD8 T
NKT
Unconv T
B
% CD8+ T (fold change)
10
1
0.1
0.0156
RTW3
RTFU
RT
CRT
C
% GrzmB+ CD8+ T (fold change)
0.0391
% CD56+ Tconv (fold change)
0.0156
D
% Ki67+ Treg (fold change)
0.0391
E
% PD-1+ CD8+ T (fold change)
0.0078
% PD-1+ Tconv (fold change)
0.0078
F
% TEX CD8+ T (fold change)
% TPEX CD8+ T (fold change)
100
0.01
0.0078